

## MOLECULAR OUTFLOWS FROM THE PROTOCLUSTER, SERPENS SOUTH

FUMITAKA NAKAMURA<sup>1,2</sup>, KOJI SUGITANI<sup>3</sup>, YOSHITO SHIMAJIRI<sup>4</sup>, TAKASHI TSUKAGOSHI<sup>5</sup>, AYA E. HIGUCHI<sup>1</sup>, SHOGO NISHIYAMA<sup>6</sup>, RYOHEI KAWABE<sup>4</sup>, MICHIIRO TAKAMI<sup>7</sup>, JENNIFER L. KARR<sup>7</sup>, ROBERT A. GUTERMUTH<sup>8</sup>, GRANT WILSON<sup>8</sup>

*Draft version January 23, 2013*

### ABSTRACT

We present the results of CO ( $J = 3 - 2$ ) and HCO<sup>+</sup> ( $J = 4 - 3$ ) mapping observations toward a nearby embedded cluster, Serpens South, using the ASTE 10 m telescope. Our CO ( $J = 3 - 2$ ) map reveals that many outflows are crowded in the dense cluster-forming clump that can be recognized as a HCO<sup>+</sup> clump with a size of  $\sim 0.2$  pc and mass of  $\sim 80 M_{\odot}$ . The clump contains several subfragments with sizes of  $\sim 0.05$  pc. By comparing the CO ( $J = 3 - 2$ ) map with the 1.1 mm dust continuum image taken by AzTEC on ASTE, we find that the spatial extents of the outflow lobes are sometimes anti-correlated with the distribution of the dense gas and some of the outflow lobes apparently collide with the dense gas. The total outflow mass, momentum, and energy are estimated at  $0.6 M_{\odot}$ ,  $8 M_{\odot} \text{ km s}^{-1}$ , and  $64 M_{\odot} \text{ km}^2 \text{ s}^{-2}$ , respectively. The energy injection rate due to the outflows is comparable to the turbulence dissipation rate in the clump, implying that the protostellar outflows can maintain the supersonic turbulence in this region. The total outflow energy seems only about 10 percent the clump gravitational energy. We conclude that the current outflow activity is not enough to destroy the whole cluster-forming clump, and therefore star formation is likely to continue for several or many local dynamical times.

*Subject headings:* ISM: clouds — ISM: jets and outflows — stars: formation — submillimeter — turbulence

### 1. INTRODUCTION

Most stars form in clusters (Lada & Lada 2003; Allen et al. 2006). Therefore, understanding the formation process of star clusters is a key step towards a full understanding of how stars form. Recent observations have revealed that star clusters form in turbulent, magnetized, parsec-scale dense clumps of molecular clouds (Ridge et al. 2003). These clumps contain masses of  $10^2 - 10^3 M_{\odot}$ , fragmenting into an assembly of cores that collapse to produce stars (e.g. Davis et al. 1999; Sandell & Knee 2001; ?; André et al. 2007; Kirk et al. 2007; Walsh et al. 2007; Saito et al. 2008; Maruta et al. 2010). In cluster-forming clumps, stellar feedback such as protostellar outflows, stellar winds, and radiation rapidly start to shape the surroundings. Because of the short separations between forming stars and cores, these feedback mechanisms are expected to control subsequent star formation (e.g., Norman & Silk 1980; Krumholz et al. 2006; McKee & Ostriker 2007; Matzner 2007; Nakamura & Li 2007; Peters et al. 2010; Wang et al. 2010). However, the roles of the stellar feed-

back on cluster formation remain poorly understood observationally.

According to recent theoretical studies, two main scenarios of cluster formation are now under debate. For these two scenarios, the roles of the stellar feedback on cluster formation are different. One is the rapid, dynamical formation model, in which the large-scale turbulent flow mainly controls star formation in cluster-forming clumps, and star formation is envisioned to complete in a short time (e.g., Elmegreen 2007; Hartmann & Burkert 2007). In this case, cluster formation is expected to be terminated by stellar feedback due to initial star burst within a couple of turbulence-crossing times, so that star formation efficiencies (SFEs) can stay low at a observed level in nearby cluster-forming regions (SFE  $\sim 0.1$ ). To promote rapid gravitational collapse and thus rapid star formation, the magnetic fields should be weak dynamically. Another scenario is the quasi-virial equilibrium model, in which cluster formation is considered to continue at least for several dynamical, or free-fall, times (e.g., Tan et al. 2006; Li & Nakamura 2006). Because supersonic turbulence dissipates rapidly in a turbulence-crossing time, additional turbulent motions should be injected to maintain the supersonic turbulence. Protostellar outflow feedback is proposed to play a significant role in the turbulence regeneration (Matzner 2007; Nakamura & Li 2007; Carroll et al. 2010). The moderately-strong magnetic fields are also important to impede the rapid global gravitational collapse. In this case, the global inflow and outflow are expected to coexist, interacting with themselves. As a result, the cluster-forming clumps as a whole can keep quasi-equilibrium states for a relatively long time.

In an effort to discriminate between the two scenarios and constrain the theory of cluster formation, we have made a start on a systematic observational study

<sup>1</sup> National Astronomical Observatory, Mitaka, Tokyo 181-8588, Japan; fumitaka.nakamura@nao.ac.jp

<sup>2</sup> Institute of Space and Astronautical Science, Japan Aerospace Exploration Agency, 3-1-1 Yoshinodai, Sagami-hara, Kanagawa 229-8510, Japan

<sup>3</sup> Graduate School of Natural Sciences, Nagoya City University, Mizuho-ku, Nagoya 467-8501, Japan

<sup>4</sup> Nobeyama Radio Observatory, Nobeyama, Minamimaki, Minamisaku, Nagano, 384-1305, Japan

<sup>5</sup> Department of Astronomy, School of Science, University of Tokyo, Bunkyo, Tokyo 113-0033, Japan

<sup>6</sup> Department of Astronomy, Kyoto University, Sakyo-ku, Kyoto 606-8502, Japan

<sup>7</sup> Academia Sinica Institute of Astronomy and Astrophysics, P.O. Box 23-141, Taipei 106, Taiwan

<sup>8</sup> Department of Astronomy, University of Massachusetts, Amherst, MA 01003, USA

of a nearby infrared dark cloud (IRDC), Serpens South, with a focus on the stellar feedback. Recent observations strongly suggest that IRDCs are in the very early phase of star cluster formation (Rathborne et al. 2006; Perreto & Fuller 2009; Butler & Tan 2009) and presumably still retain the primordial structure of the cluster’s natal cloud. In particular, in the early phase of evolution, the protostellar outflows are likely to play a more dominant role in cloud dynamics, compared to the stellar winds and radiation, because they are more powerful in the early protostellar evolution (Bontemps et al. 1996). Therefore, IRDCs are expected to be suitable to explore the roles of protostellar outflows on cluster formation.

Serpens South is a nearby embedded cluster, recently discovered by Gutermuth et al. (2008) using the Spitzer Space telescope. The accurate distance to Serpens South remains unknown. Most of the previous studies adopt the same distance as the Serpens Cloud Core, located about  $3^\circ$  north, because the YSOs associated with Serpens South have the same LSR velocities as the Serpens Cloud Core, whose distance is usually adopted as  $260 \pm 37$  pc (Straizys et al. 1996). However, larger distances of  $415 \pm 25$  pc, 380 pc, and  $360^{+22}_{-13}$  pc have been recently claimed for the Serpens Cloud Core based on a VLBA parallax of EC95, a young AeBe star embedded in Serpens Cloud Core (Dzib et al. 2010), SEDs of YSOs based on the near infrared observations (Gorlova et al. 2010), and X-ray luminosity functions (Winston et al. 2010), respectively. According to Gutermuth et al. (2008), the Serpens South cloud appears to be seen in absorption against PAH emission from the W40 HII region. Therefore, the distance to W40 is likely to be an upper limit to the distance to Serpens South, although even the former has not yet been determined to any satisfactory precision (300 pc – 900 pc; Rodney & Reipurth 2008). In this paper, we assume 260 pc as the distance to Serpens South.

From the Spitzer IRAC observations, Gutermuth et al. (2008) revealed that the cluster contains about 60 Class I protostars and 40 Class II sources. Recently, Bontemps et al. (2010) have discovered 7 Class 0 candidates in this region through the Herschel Gould Belt Survey (see André et al. 2010). In the central part of the cluster, the fraction of Class I protostars relative to all the YSOs (Class I/II) reaches about 80 % at the high surface density of  $430 \text{ pc}^{-2}$ . These observations indicate that Serpens South is undoubtedly in the very early stage of cluster formation, i.e., Serpens South is a “protocluster” that are forming a number of stars. Gutermuth et al. (2008) also estimated the median projected distance between nearest neighbor YSOs to be about 3700 AU, significantly shorter than the typical length of protostellar outflow lobes, implying that the outflows can potentially influence star formation in this region.

Recent dust continuum observations have revealed that the cluster is located at the constricted region in a long filamentary cloud that is recognized as a dark cloud in mid-infrared ( $\sim 10 \mu\text{m}$ ) wavelength (Gutermuth et al. 2008, 2011; André et al. 2010). Several sub-filaments also appear to converge toward the main filament (e.g. Myers 2009; Bontemps et al. 2010). Very recently, Sugitani et al. (2011) carried out near-infrared (JHKs)

polarization observations toward Serpens South using the imaging polarimeter SIRPOL which is a polarimetry mode of the near-infrared camera SIRIUS mounted on the IRSF 1.4 m telescope at the South Africa Astronomical Observatory. They found that the global magnetic field is spatially well-ordered and almost perpendicular to the main filament. Several sub-filaments appear to be parallel to the global magnetic field. These observational facts imply that moderately-strong magnetic field played a role in the course of the formation of the Serpens South filament. The moderately-strong magnetic field appears consistent with the quasi-virial equilibrium model where the magnetic fields significantly impede the global gravitational collapse (see, e.g., Nakamura & Li 2011). In this paper, we investigate the outflow activity in the Serpens South cloud on the basis of the CO ( $J = 3 - 2$ ) and HCO<sup>+</sup> ( $J = 4 - 3$ ) observations using the ASTE 10 m telescope.

The rest of the paper is organized as follows. First, we describe the details of our CO ( $J = 3 - 2$ ) and HCO<sup>+</sup> ( $J = 4 - 3$ ) observations toward Serpens South in Section 2. We present in Section 3 our CO ( $J = 3 - 2$ ) and HCO<sup>+</sup> ( $J = 4 - 3$ ) maps toward Serpens South, which reveal a number of powerful collimated outflows and clumpy structure in the central part of the protocluster, respectively. We also compare our CO ( $J = 3 - 2$ ) map with the three-color Spitzer IRAC image ( $3.6 \mu\text{m}$  in blue,  $4.5 \mu\text{m}$  in green,  $8.0 \mu\text{m}$  in red) to help identify the molecular outflow lobes. In the three-color image, the knots created by shocks due to the outflows are found as extended green objects with excess in  $4.5 \mu\text{m}$  emission (e.g., Takami et al. 2010). We derive the global properties of the outflows identified from our CO ( $J = 3 - 2$ ) map. Then, in Section 4, we briefly discuss how the observed outflows influence the clump dynamics. Finally, we summarize our main conclusion in Section 5.

## 2. OBSERVATIONS

The CO ( $J = 3 - 2$ ; 345.796GHz) and HCO<sup>+</sup> ( $J = 4 - 3$ ; 356.734GHz) mapping observations were carried out with the ASTE 10 m telescope (Ezawa et al. 2004) toward Serpens South during the period of August 12 – 14 2010, using the on-the-fly (OTF) mapping technique (Sawada et al. 2008). Figure 1 presents the observation boxes that are overlaid on the column density map derived from the Herschel observations (André et al. 2010), indicating that our observation area covers most of the dense filamentary structure associated with Serpens South. Our main observation box (Box 1 in Fig. 1) covers a  $13' \times 13'$  region centered at the dense part of the protocluster, (RA, Dec) = (18h30m3.4s,  $-2^\circ 2' 4.6''$ ). We make the image, by combining scans along the two axes that run at right angles to one another using the PLAIF algorithm developed by Emerson & Graeve (1988), in order to minimize the “scanning effect”. The observation region was extended to a larger  $20' \times 20'$  box (Box 2 in Fig. 1). We also observed a  $13' \times 13'$  box (Box 3 in Fig. 1) centered on (RA, Dec) = (18h29m16s,  $-1^\circ 41' 35''$ ). The extended observation areas (Boxes 2 and 3) have higher noises and suffer from the scanning effects due to the OTF observations because only one scan was done. The beam size in HPBW of the ASTE telescope is  $22''$ , which corresponds to 0.028 pc at a distance of 260 pc. The main-beam efficiency,  $\eta$ , was 0.57 at 345 GHz. We used

a 345 GHz SIS heterodyne receiver, which had the typical system noise temperature of about 200 K in DSB mode at the observed elevation. The temperature scale was determined by the chopper-wheel method, which provides us with the antenna temperature,  $T_A^*$ , corrected for the atmospheric attenuation. As a backend, we used four sets of 1024 channel autocorrelators, providing us with a frequency resolution of 125 KHz that corresponds to 0.11 km s<sup>-1</sup> at 345 GHz. After subtracting linear baselines, the data were convolved with a Gaussian-tapered Bessel function (Magnum et al. 2007) and were resampled onto a 5'' grid. The resultant effective FWHM resolution is 24''. The typical rms noise levels are 0.11 K and 0.51 K in  $T_A^*$  with a velocity resolution of 0.5 km s<sup>-1</sup> for Box 1 and Box 2 and 3, respectively.

As for the Spitzer IRAC data, archival data in three IRAC bands (3.6, 4.5, and 8.0  $\mu$ m) were obtained for Serpens South. All the data had been reduced with the basic calibration data (BCD) pipelines developed by Infrared Processing and Analysis Center (IPAC), and mosaicked with the MOsaicking and Point Source Extraction (MOPEX) software developed by Spitzer Science Center. The mean FWHMs of the point response functions (PRFs) are 1''.66, 1''.72, 1''.98, for the three bands, respectively (See Spitzer Space Telescope Observer's Manual Version 8.0).

### 3. RESULTS

#### 3.1. Global Cloud Properties

Since both the CO ( $J = 3 - 2$ ) and HCO<sup>+</sup> ( $J = 4 - 3$ ) transitions have higher critical densities (approximately,  $10^4$  and  $10^7$  cm<sup>-3</sup>, respectively) and higher transition energies ( $\sim 33$  and 43 K, respectively) than those of the lower transition lines such as CO ( $J = 1 - 0$ ), it allows us to examine higher density and/or higher temperature gas. In Figure 2, we present the CO ( $J = 3 - 2$ ) velocity integrated intensity map in the ranges from  $v_{\text{LSR}} = -2$  km s<sup>-1</sup> to  $+15$  km s<sup>-1</sup>, which shows that the CO ( $J = 3 - 2$ ) emission tends to be much stronger in the southern box with about  $20' \times 20'$  area (Boxes 1 and 2), while a relatively weak emission can be seen in the northern box with about  $13' \times 13'$  area (Box 3). In fact, the Serpens South protocluster resides in Box 1, and the strong CO ( $J = 3 - 2$ ) emission originates mainly from the powerful molecular outflows of the cluster member YSOs, as described in the next subsection. We note that the weak CO ( $J = 3 - 2$ ) emission was detected in the entire observed area, indicating that the molecular gas is widely distributed in much larger area.

We also present in Figures 3a, 3b, and 3c, the CO ( $J = 3 - 2$ ) peak intensity, HCO<sup>+</sup> ( $J = 4 - 3$ ) peak intensity, and 1.1 mm continuum maps, respectively, toward Box 2. The 1.1 mm continuum map was taken by the AzTEC camera (Wilson et al. 2008) on the ASTE 10 m telescope (Gutermuth et al. 2011). The positions of Class I and II sources identified by Gutermuth et al. (2008) from the Spitzer IRAC observations are plotted in Figures 3a through 3c. The 1.1 mm map indicates that the dense gas is distributed along a long filament running from north to south. This filament (hereafter, the main filament) has several sub-filaments that appear to converge toward the main filament. Such structures appear to be common in many star-forming region, as

pointed out by Myers (2009).

The CO ( $J = 3 - 2$ ) peak intensity map in Fig. 2a is not dominated by emission at the systemic velocity of the cloud,  $\sim 7.5$  km s<sup>-1</sup>. Such a feature is prominent in the velocity channel maps presented in Figs. 4 and 5, where the emission is weak in the range from  $\sim 7$  to  $\sim 10$  km s<sup>-1</sup>. For comparison, we also present in Figures 6 and 7 the CO ( $J = 3 - 2$ ) and HCO<sup>+</sup> ( $J = 4 - 3$ ) spectra, respectively. The CO ( $J = 3 - 2$ ) spectra often show double-peak line profiles, whereas the HCO<sup>+</sup> ( $J = 4 - 3$ ) spectra often show single-peak line profiles. By comparing the CO ( $J = 3 - 2$ ) and HCO<sup>+</sup> ( $J = 4 - 3$ ) spectra, it is clear that the CO ( $J = 3 - 2$ ) line profiles appear to be caused by self-absorption in the range from  $\sim 7$  to  $\sim 10$  km s<sup>-1</sup>, rather than multiple velocity components.

Strong CO ( $J = 3 - 2$ ) and HCO<sup>+</sup> ( $J = 4 - 3$ ) emission come from almost the same part where the 1.1 mm emission is strongest and the Serpens South protocluster is located. In fact, the CO ( $J = 3 - 2$ ) and HCO<sup>+</sup> ( $J = 4 - 3$ ) emission peaks coincide reasonably well with the 1.1 mm peak. The HCO<sup>+</sup> ( $J = 4 - 3$ ) emission is distributed in an elongated clump with the axis ratio of about 1.5–2. The HCO<sup>+</sup> ( $J = 4 - 3$ ) integrated intensity map presented in Fig. 7 suggests that the clump contains several subfragments. The clumpy structure of the HCO<sup>+</sup> clump is more evident in the HCO<sup>+</sup> ( $J = 4 - 3$ ) velocity channel maps presented in Fig. 8. The typical size of the subfragments is about 0.05 pc. The positions of two subfragments (sources 1 and 2 indicated in Fig. 11b) are indicated by the diamonds in Fig. 8. As shown in the next subsection, these two subfragments contain the possible driving sources of the outflows. The HCO<sup>+</sup> ( $J = 4 - 3$ ) emission takes its maximum at the position of source 2 presented in Fig. 11 that coincides with the position of the 1.1 mm peak. The positions of these two subfragments coincide reasonably well with those of the 3 mm compact sources recently identified by the NMA observations (Fukuda et al. in prep.).

The CO line profiles have prominent blueshifted and/or redshifted wings near the region where the CO emission is strongest, as can be seen in Fig. 6. The line wings sometimes extend over the velocity range of  $-10 \sim 30$  km s<sup>-1</sup>. These prominent wings indicate the presence of powerful molecular outflows in this region. The CO ( $J = 3 - 2$ ) peak intensity map indicates that there are several local peaks and ridges near the central dense part of the protocluster. As shown in Section 3.2, these peaks trace the outflow lobes reasonably well. Similar high-velocity wings can also be seen in the HCO<sup>+</sup> ( $J = 4 - 3$ ) line profiles (see Fig. 7) that are sometimes extended in the range from about 3 km s<sup>-1</sup> to 15 km s<sup>-1</sup> around the subfragments located near the 1.1 mm peak.

In the southern part of Box 2, the redshifted components of the identified outflows tend to be extremely weak (see also the line profiles presented in Fig. 6b). It is unclear what causes the extremely-asymmetric line profiles in the southern area. One possibility is the existence of a foreground cloud in the velocity of around 10 km s<sup>-1</sup> in the southern area. The foreground cloud, if cold, preferentially absorbs the redshifted outflow components. Another possibility is the existence of the global

infall toward the southern part of the cloud. If the cloud envelope is infalling, the foreground infall gas having velocities similar to the redshifted outflow components can absorb the redshifted components. In the next subsection, we identify the molecular outflow lobes from CO ( $J = 3 - 2$ ) data and discuss several features of the outflow lobes in detail.

### 3.2. Molecular Outflows

Here, using the CO ( $J = 3 - 2$ ) data cubes, we attempt to identify high-velocity components that originate from molecular outflows. First, we scrutinize the velocity channel maps (Figs. 4 and 5) and the position-velocity diagrams (see e.g., Fig. 17) to find localized blueshifted or redshifted emission. As can be seen in Figs. 4 and 5, the  $^{12}\text{CO}$  high velocity structure is very complex and crowded in the southern box with about  $20' \times 20'$  area (Box 2). Thus, identifying outflows from the  $^{12}\text{CO}$  emission alone is extremely difficult in this crowded area. Therefore, we compare the CO image with three-color Spitzer IRAC images ( $3.6 \mu\text{m}$  in blue,  $4.5 \mu\text{m}$  in green,  $8.0 \mu\text{m}$  in red) of this region, which are presented in Figure 10. The blow-up of the central area is shown in Figure 11. According to previous studies (e.g., Noriega-Crespo et al. 2004; Takami et al. 2010), extended objects that have strong emission in IRAC channel 2 ( $4.5 \mu\text{m}$ ) compared to IRAC channel 1 ( $3.6 \mu\text{m}$ ) and stand out as extended green objects in the three-color images are likely to be the objects shocked by the protostellar outflows. Here, we refer to such objects as infrared H-H objects. To identify the infrared H-H objects, we first made an image of the remaining emission in the Spitzer IRAC band 2 ( $4.5 \mu\text{m}$ ) image after the subtraction of the emission in band 1 ( $3.6 \mu\text{m}$ ). This image processing in practice allows us to discriminate between shocks and stars, displaying them with positive and negative values, respectively (Zhang & Wang 2009; Takami et al. 2010). We then visually inspected the image to search for mid-infrared outflows. We selected spatially-extended sources that have significant excess at  $4.5 \mu\text{m}$  as mid-infrared outflows. The positions of the identified infrared H-H objects are indicated by the crosses in Figs. 10b, 11b, and 12b. Some of the infrared H-H objects have bow-shapes. For example, the infrared H-H objects labeled as K1 and K2 in Fig. 12a have arc-like features, both of which appear to move toward the south west direction (see Figs. 13a and 12b). From our CO ( $J = 3 - 2$ ) and Spitzer IRAC data, we identified 15 blueshifted and 10 redshifted components. The positions of the identified lobes are indicated in Fig. 9. Table 1 gives a brief summary of the identified outflow lobes. We also show in Fig. 16 the blueshifted and redshifted high-velocity components identified from  $\text{HCO}^+$  ( $J = 4 - 3$ ). In the following, we describe some of the main features of the high-velocity components we identified from the CO ( $J = 3 - 2$ ) data.

The relatively strong blueshifted components B1 and B4 are well localized in the channel maps and appear at the maps within the wide range of  $0.75 \text{ km s}^{-1}$  to  $5.75 \text{ km s}^{-1}$ . These lobes have extremely high-velocity blueshifted components. In particular, the B1 component has moderately-strong emission even in the velocity range of about  $-10 \text{ km s}^{-1}$  (see Fig. 6). There are also many infrared H-H objects associated with these two

components. The B1 and B4 appear to move away from the central dense part toward north and south, respectively. In fact, the most distant infrared H-H object associated with B4 has a bow shape, consistent with the interpretation that it is moving away from the dense part (see Fig. 11b). As mentioned below, the B4 component might originate from a compact 3 mm source located at the 1.1 mm peak, recently identified by the Nobeyama Millimeter Array (NMA) observations (Fukuda et al. in prep.). If this is the case, the corresponding redshifted components are likely to be R2 and R3. The position of the 1.1 mm peak is indicated by a diamond (source 2 in Fig. 11b) in the Spitzer image. It appears that no clear Spitzer sources are associated with the 1.1 mm peak. The 3 mm source discovered by the NMA observations may be a deeply-embedded, extremely-young protostar such as a Class 0 source. In fact, the  $\text{HCO}^+$  ( $J = 4 - 3$ ) line profile toward source 2 shows blue-shifted part that are stronger than the red-shifted part (see Fig. 14). Such a blue-skewed profile of an optically-thick line may be indicative of infalling gas, suggesting that the 3 mm source located at the 1.1 mm peak is an infalling object having a powerful outflow.

There are two faint blueshifted components labeled with B2 and B3. They are vaguely seen in the channel maps with high velocities ( $0.75 \text{ km s}^{-1} \sim 1.75 \text{ km s}^{-1}$ ). Some infrared H-H objects appear to be associated with the B3 component (see Fig. 11). The position-velocity diagram indicates that the blueshifted component B8 is likely to be the outflow component that appears to move away toward south. The blueshifted components B14 and B7 are located near the edge of Box 1. Although B7 appears to move from north west to south east from its morphology, the driving source remains unknown. There is no redshifted counterpart associated with B7. The B7 component is also associated with some extended green objects suggesting that the ambient gas is shocked by the B7 component (see Fig. 12). The B14 component also do not have a redshifted counterpart. There is a compact dust continuum source immediately south of B14, where Bontemps et al. (2010) found two protostar candidates by the Herschel observations. The Spitzer image also shows two compact sources at the same places as the dust continuum source and the Herschel protostar candidates (Fig. 12). We suggest that the northern source is likely to be the driving source of B14. This interpretation appears to be supported by the fact that the 1.1 mm emission is weak at the position of the B14 component, apparently breaking the main filament into two parts (see Fig. 15a), and bending the northern part of the filament toward south. There are some infrared H-H objects in the southern part of B14. These objects may originate from B14.

The relatively-faint blueshifted component B6 is clearly seen in the channel maps in the range of  $3 \text{ km s}^{-1}$  to  $5 \text{ km s}^{-1}$ , apparently moving toward the south-west direction. The possible driving source is one of the Class I sources identified by Gutermuth et al. (2008) (source 3 in Fig. 11) because some H-H objects appear to be ejected from it. The B6 component appears to point toward the relatively-strong blueshifted component B9. However, it is unclear whether B9 originates from the outflow lobe. The peak of B9 is about 0.4 pc away from the 1.1 mm peak. The position-velocity diagram may imply that this

component has different LSR velocity ( $V_{\text{LSR}} \sim 2 \text{ km s}^{-1}$ ) from the central dense part and does not show the velocity structure typical of the outflow lobe (see Fig. 17b). However, there are no YSOs associated with the same area as the B9 component. Therefore, this component might be a fossil of the outflow lobe or infalling gas toward the central dense part along a sub-filament. Further investigation is needed to clarify the origin of this component.

There is a redshifted component R1 between the two blueshifted components B1 and B2. This redshifted component is clearly seen in the peak intensity map and appears to move away from the dense part. This component appears to be associated with a blueshifted component, which can be seen in the velocity channel maps with  $4.75 \text{ km s}^{-1}$  and  $5.75 \text{ km s}^{-1}$ . Therefore, this component may be almost parallel to the plane-of-sky direction. The possible driving source is indicated by a diamond in Fig. 11a (source 1), from which many H-H objects are apparently ejected.

The strong redshifted components R2 and R3 appear to move away from the central dense part, clearly showing the velocity structure typical of the outflow components. Several infrared H-H objects are associated with these components. Interestingly, at the area between R2 and R3, the 1.1 mm emission shows a double-peak feature and the 1.1 mm emission tends to be weak on the line connecting between R2 and R3 (see Fig. 15b). In addition, there is an area having relatively strong 1.1 mm emission just at the north of R2. This morphology leads us to the following possibility: the redshifted lobes R2 and R3 come from the same source and R2 went through the dense part, reaching and hitting the dense part located at the north. The R3 component appears to coincide with the high-velocity component identified by the  $\text{HCO}^+$  ( $J = 4 - 3$ ) map (see Fig. 16). Such high-velocity dense gas may suggest that the outflow is very young. As mentioned above, the possible driving source is a 3 mm source recently discovered by the NMA observations, whose position almost coincides with the 1.1 mm peak (source 2 in Fig. 11, Fukuda et al. in prep.). However, other unknown sources might be the real driving sources of these outflow lobes because this central part is very dense and crowded.

There is a faint redshifted component R4 in the south west part of the dense part. Several infrared H-H objects are associated with the R4 component. This component is clearly seen in the channel maps with  $11.75$  through  $13.75 \text{ km s}^{-1}$ , apparently moving toward the south-west direction. In fact, the most distant infrared H-H object (K2 in Fig. 13b) has a bow shape, consistent with the interpretation that it is moving away from the dense part. Since a faint blueshifted component labeled by B5 is associated with the R4 component, this component might be almost parallel to the plane-of-sky. The possible driving source is one of the Class I objects identified by Gutermuth et al. (2008) (source 4 in Fig. 11) because some infrared H-H objects are apparently ejected from it.

Several bipolar outflows can be identified clearly in the CO ( $J = 3 - 2$ ) data. For example, the southernmost outflow with the B15 and R8 lobes looks relatively powerful and clearly shows a bipolar feature. The driving source is probably one of the Herschel candidate protostars identified by Bontemps et al. (2010) (see their Fig. 5) whose

position is (RA, Dec)  $\simeq (18\text{h}30\text{m}2\text{s}, -2^\circ10'20'')$ . The candidate protostar is also seen in the 1.1 mm continuum image presented in Fig. 15b and the Spitzer IRAC image in Fig. 10, as a point-like source. Another bipolar outflow can be seen near the upper right corner of panel (c) of Fig. 9. The driving source may be either a Herschel candidate protostar or a Class 0 object located at the upper-right corner of Fig. 5 of Bontemps et al. (2010). In the northern box with about  $13' \times 13'$  area (Box 3) we found three molecular outflows, all of which show clear bipolar features: B10 and R5, B11 and R6, and B12 and R7. Since this region is out of our Spitzer image, we cannot identify the driving sources.

In Box 2, we identified four additional high-velocity components labeled by B13 and R9. These components possibly originate from some outflows. However, further observations would be needed to clearly identify the outflow lobes.

We note that the directions of the outflow lobes often appear to be roughly along the global magnetic field direction that is running almost perpendicularly to the main filament (Sugitani et al. 2011), e.g., B2, B5, B6, B9, B15, B16, R4, R8, and R10. However, several components, e.g., B1, B3, B4, R2, and R3, appear to be independent of the global magnetic field direction. This indicates that the central dense part is magnetically supercritical and therefore, the local supersonic turbulence have presumably perturbed the magnetic field significantly. In fact, the recent numerical simulations of cluster formation indicate that even the moderately-strong magnetic field causes a significant misalignment between the global field direction and the outflow propagation directions because of the strong turbulence (Nakamura & Li 2011).

### 3.3. Derivation of the Physical Quantities

#### 3.3.1. Outflow Parameters

Figure 9 shows that the high-velocity components are crowded in the central dense part where the protocluster resides and therefore it is very difficult to clearly discriminate the individual outflow lobes from the data. Therefore, we postpone to accurately evaluate the physical properties of the individual outflows until high spatial resolution data taken by interferometric observations become available. In the following, we calculate some global physical properties of the outflowing gas located at the cluster center. On the other hand, five bipolar outflows mentioned in the previous subsection can be easily identified in the CO ( $J = 3 - 2$ ) map, because they are found in relative isolation. However, we postpone to calculate the individual outflow parameters of these bipolar outflows because the rms noise level is relatively high with a significant scanning effect, precluding accurate estimation of the outflow parameters.

Examination of the spectra in the cloud shows that ambient  $^{12}\text{CO}$  spectra away from the outflows appear to cover a velocity range of  $6$  to  $11 \text{ km s}^{-1}$ . We thus assume that the emission in this velocity range include ambient emission for the entire cloud. Therefore, the integration ranges used are  $-15$  to  $4 \text{ km s}^{-1}$  for the blue-shifted emission and  $11$  to  $30 \text{ km s}^{-1}$  for the red-shifted emission, respectively. The outflow masses were calculated under the assumption of LTE, a distance of  $260 \text{ pc}$ , and

optically-thin emission in the line wings with an excitation temperature of 30K. We note that the physical quantities estimated below are insensitive to the excitation temperature. The estimated quantities increase only by 20 % over the range of  $T_{\text{ex}} = 20 - 50$  K.

Following Nakamura et al. (2011), the outflow mass  $M_{\text{out}}$ , the outflow momentum  $P_{\text{out}}$ , and kinetic energy  $E_{\text{out}}$  are estimated as

$$M_{\text{out}} = \sum_j M_j, \quad (1)$$

$$P_{\text{out}} = \sum_j M_j |V_j - V_{\text{sys}}| / \cos \xi, \quad (2)$$

and

$$E_{\text{out}} = \sum_j \frac{1}{2} M_j (V_j - V_{\text{sys}})^2 / \cos^2 \xi, \quad (3)$$

respectively, where  $M_j$  is the mass of the  $j$ -th channel,  $V_j$  is the LSR velocity of the  $j$ -th channel and  $V_{\text{sys}}$  is the systemic velocity of the driving source. Here, we adopt  $V_{\text{sys}} = 7.5 \text{ km s}^{-1}$ . The angle  $\xi$  is the inclination angle of an outflow, which is generally uncertain. Here, we adopt  $\xi = 57.3^\circ$ , following Bontemps et al. (1996). The mass of the  $j$ -th channel,  $M_j$ , is expressed as

$$\begin{aligned} M_j &= \mu_g m_{\text{H}_2} X_{\text{CO}}^{-1} \Omega D^2 \sum_i N_{\text{CO},i,j} \\ &= 3.2 \times 10^{-9} \left( \frac{X_{\text{CO}}}{10^{-4}} \right)^{-1} \left( \frac{D}{260 \text{ pc}} \right)^2 \left( \frac{\Delta \theta}{\text{arcsec}} \right)^2 \\ &\quad \times \left( \frac{\eta}{0.57} \right)^{-1} \left( \frac{\sum_i T_{A,i,j}^* \Delta v}{\text{K km s}^{-1}} \right) T_{\text{ex}} \exp \left[ \frac{33.2 \text{ K}}{T_{\text{ex}}} \right] M_{\odot} \end{aligned} \quad (4)$$

where  $i$  is the grid index on the  $j$ -th channel,  $N_{\text{CO},i,j}$  is the CO column density at the  $i$ -th grid on the  $j$ -th channel,  $\eta$  ( $=0.57$ ) is the main beam efficiency of the ASTE telescope,  $m_{\text{H}_2}$  is the mass of a hydrogen molecule,  $X_{\text{CO}}$  is the fractional abundance of CO relative to  $\text{H}_2$ , and the mean atomic weight of the gas  $\mu_g$  is set to 1.36. We adopt  $X_{\text{CO}} = 10^{-4}$ .  $\Omega$  is the solid angle of the object and  $D$  is the distance to the object. From these quantities, we calculate the characteristic velocity as  $V_{\text{out}} = P_{\text{out}}/M_{\text{out}}$ .

Table 2 summarizes the outflow parameters derived from the CO ( $J = 3 - 2$ ) data. The physical quantities presented in Table 2 depend on the adopted velocity interval for the integration. For example, if we change the velocity intervals as  $-15$  to  $6 \text{ km s}^{-1}$  ( $-15$  to  $2 \text{ km s}^{-1}$ ) for the blue-shifted emission and  $9$  to  $30 \text{ km s}^{-1}$  ( $13$  to  $30 \text{ km s}^{-1}$ ) for the red-shifted emission, the total mass, momentum, and energy change by  $+65\%$  ( $-50\%$ ),  $20\%$  ( $-30\%$ ), and  $5\%$  ( $-13\%$ ), respectively. This indicates that the total momentum and energy do not depend strongly on the adopted velocity intervals, although the total mass does. This is probably due to the fact that the outflow components with lower velocities have lower momenta and kinetic energies. As mentioned above, the distance to Serpens South remains uncertain. If we adopt  $D = 410 \text{ pc}$  (e.g., Dzib et al. 2010), instead of  $260 \text{ pc}$ , then the mass, momentum, and energy increase further by a factor of 2.5. Therefore, a main uncertainty on the estimation of the outflow parameters comes from the

adopted distance to the cloud, rather than the adopted velocity intervals.

### 3.3.2. Mass of Dense Clump

The  $\text{HCO}^+$  ( $J = 4 - 3$ ) line emission has a critical density of  $10^7 \text{ cm}^{-3}$ , and thus traces the dense molecular gas. Here, we estimate the mass and radius of the central dense clump, using the  $\text{HCO}^+$  ( $J = 4 - 3$ ) data (see Fig. 7a). The mass of the  $\text{HCO}^+$  ( $J = 4 - 3$ ) is evaluated from

$$\begin{aligned} M &= \mu_g m_{\text{H}_2} X_{\text{HCO}^+}^{-1} \Omega D^2 \sum_i N_{\text{HCO}^+,i,j} \\ &= 3.1 \times 10^{-8} \left( \frac{X_{\text{HCO}^+}}{1.2 \times 10^{-9}} \right)^{-1} \left( \frac{D}{260 \text{ pc}} \right)^2 \left( \frac{\Delta \theta}{\text{arcsec}} \right)^2 \\ &\quad \times \left( \frac{\eta}{0.57} \right)^{-1} \left( \frac{\sum_i T_{A,i,j}^* \Delta v}{\text{K km s}^{-1}} \right) T_{\text{ex}} \exp \left[ \frac{43 \text{ K}}{T_{\text{ex}}} \right] M_{\odot} \end{aligned} \quad (5)$$

From the above expression, the mass and radius of the central clump are estimated to be about  $80 M_{\odot}$  and  $0.1 \text{ pc}$ , respectively, where we assumed LTE and the excitation temperature of  $14 \text{ K}$  (André et al. 2010). The mean density is estimated to be  $M_{\text{clump}}/(4\pi R_{\text{clump}}^3/3) \sim (3-7) \times 10^5 \text{ cm}^{-3}$ . The estimated mean density is smaller than the critical density of the  $\text{HCO}^+$  ( $J = 4 - 3$ ) line by an order of magnitude. This may suggest that the central clump contains multiple small subfragments that are not spatially-resolved in our observation. In fact, recent numerical simulations of cluster formation suggest that the central dense region of a cluster forming clump consists of multiple thin filaments that tend to fragment into denser blobs by the destruction due to the outflow feedback (Li et al. 2010). However, it is difficult to verify such a clumpy structure only from our observations. Higher spatial resolution observations will be needed to reveal the density structure of the dense clump. The fractional abundance of  $\text{HCO}^+$  relative to  $\text{H}_2$  is assumed to be  $1.2 \times 10^{-9}$ , which is adopted from Maruta et al. (2010). We note that the fractional abundance of the  $\text{HCO}^+$  remains uncertain toward Serpens South. However, from the  $1.1 \text{ mm}$  data, the  $1.1 \text{ mm}$  mass in the same area as that of the  $\text{HCO}^+$  clump is evaluated to be  $\sim 10^2 M_{\odot}$ , which is not far from the mass estimated from the  $\text{HCO}^+$  emission. Therefore, the adopted  $\text{HCO}^+$  abundance is likely to be reasonable. The FWHM one-dimensional velocity width of  $\text{HCO}^+$  is estimated to be  $\Delta V \simeq 2.5 - 3.0 \text{ km s}^{-1}$  near the cluster center. The estimated velocity width corresponds to the Mach number of about 5.

## 4. DISCUSSION

According to recent theoretical studies, two main scenarios for cluster formation are proposed. One is the rapid, dynamical formation model, in which the large-scale flow mainly controls the formation of cluster-forming clumps. Star formation is considered to complete rapidly within a few crossing times before initial turbulence decays significantly (Hartmann & Burkert 2007). In this model, the magnetic field is expected to be dynamically weak to promote rapid global gravitational collapse. To terminate cluster formation, this model envisions the stellar feedback by the initial star burst that

disperses the dense gas away from the parent clumps, and eventually the clumps are destroyed.

The second scenario is the quasi-equilibrium model. In this model, star formation process is considered to be slow and continue at least for several dynamical times (Tan et al. 2006; Li & Nakamura 2006; Matzner 2007). Because supersonic turbulence dissipates quickly in a turbulence-crossing time (Stone et al. 1998; Mac Low 1999), additional turbulent motions should be injected to maintain the supersonic turbulence. In cluster-forming clumps, protostellar outflow feedback is considered to be a plausible way of driving a significant fraction of supersonic turbulence (Li & Nakamura 2006; Matzner 2007; Nakamura & Li 2007; Carroll et al. 2010). The protostellar outflow-driven turbulence can maintain the clump close to a quasi-virial equilibrium at least for several dynamical times (Matzner 2007; Nakamura & Li 2007; Carroll et al. 2010). The magnetic field is expected to be dynamically important to impede rapid global gravitational collapse. Very recently, Sugitani et al. (2011) found that the global magnetic fields associated with the Serpens South filament are well ordered, implying that the moderately-strong magnetic field played an important role in the formation of the filament. The magnetic structure is likely to be consistent with the quasi-equilibrium model.

To further constrain these cluster formation models, it is thus important to clarify the dynamical state of the clump and the energy budget of the current outflows in this region, because these two cluster formation models predict the very different star formation duration timescales. In the following, we attempt to estimate the injection rate of the turbulent energy due to the outflows and the dynamical state of the dense clump.

#### 4.1. Turbulence Dissipation and Generation

Following Nakamura et al. (2011), we estimate the total energy injection rate (mechanical luminosity) due to the protostellar outflows and energy dissipation rate of supersonic turbulence in the dense clump. From Fig. 9, the mean length of the outflow lobes can be estimated to be 0.1 - 0.2 pc, and the mean velocity along the line-of-sight direction is about 7 km s<sup>-1</sup> (see Table 2). From these values, the mean dynamical time of the outflows,  $t_{\text{dyn}}$ , can be evaluated as  $(1 - 2) \times 10^4$  years, assuming  $\xi = 57.3^\circ$ . Thus, the total energy injection rate due to the outflows is obtained as

$$L_{\text{out}} \sim E_{\text{out}}/t_{\text{dyn}} \sim (0.5 - 1)L_{\odot}. \quad (6)$$

On the other hand, the energy dissipation rate of supersonic turbulence is estimated to

$$L_{\text{turb}} \simeq C \frac{1/2 M \Delta V^2}{\lambda_d / \Delta V} \quad (7)$$

where  $C (\simeq 0.33)$  is the nondimensional coefficient,  $\Delta V$  is the one-dimensional (1D) FWHM velocity width corrected for the contribution of the thermal pressure assuming the temperature of 14 K (see Equation [3] of Maruta et al. (2010)), and  $\lambda_d$  is the driving scale of supersonic turbulence. From the HCO<sup>+</sup> ( $J = 4 - 3$ ) data, we can derive the energy dissipation rate as

$$L_{\text{turb}} \simeq 0.1 - 0.3 L_{\odot}, \quad (8)$$

where we adopted the velocity width and the driving scale  $\lambda_d$  as  $\Delta V \sim 2.5 - 3.0$  km s<sup>-1</sup> and the clump diameter of 0.2 - 0.4 pc, respectively. Both the energy injection rate  $L_{\text{out}}$  and energy dissipation rate  $L_{\text{turb}}$  are proportional to the distance to the cloud,  $D$ . Therefore, the relative importance between  $L_{\text{out}}$  and  $L_{\text{turb}}$  is irrespective of the distance uncertainty. The energy injection rate due to the outflows is somewhat larger than the energy dissipation rate. Therefore, we conclude that the outflow feedback can contribute significantly to the generation of supersonic turbulence in the clump.

Since we identified about 5 pairs of the outflows in the densest part, the mean outflow momentum for a single outflow may be estimated to be about 2 M<sub>⊙</sub> km s<sup>-1</sup>. If we assume the median stellar mass of 0.5 M<sub>⊙</sub>, then this gives the outflow momentum per unit stellar mass of about 4 km s<sup>-1</sup>, corresponding to the non-dimensional parameter  $f$  of about 0.04 (see also Maury et al. 2009 for the case of NGC2264-C), which gauges the strength of a outflow, where the wind velocity of 100 km s<sup>-1</sup> is adopted. This value is somewhat smaller than the fiducial values adopted by Matzner & McKee (2000), Li & Nakamura (2006), and Nakamura & Li (2007). The estimated value may be somewhat underestimated because the outflow lobes are assumed to be optically-thin. If the effect of the optical depth is taken into account, the value of  $f$  is presumably larger than the estimated value by a factor of a few. Even for a small value of  $f \sim 0.1$ , Nakamura & Li (2007) demonstrated that the outflow feedback can supply sufficient momentum to dynamically support a parsec-scale cluster-forming clump for several free-fall times, by means of the 3D MHD turbulent simulations. We note that if the distance to Serpens South is as large as about 900 pc, the upper limit of the distance to W40 (Rodney & Reipurth 2008), the outflow strength  $f$  is estimated to be  $f \sim 0.4$ .

#### 4.2. Dynamical State of Dense Clump

In the following, we investigate the dynamical state of the Serpens South clump, by applying the virial analysis. The virial equation for a sphere is given by

$$\frac{1}{2} \frac{\partial^2 I}{\partial t^2} = 2U + W, \quad (9)$$

where the terms,  $I$ ,  $U$ , and  $W$ , denote the moment of inertia, internal kinetic energy, and gravitational energy, respectively. For simplicity, we neglect the surface pressure term. A clump is in virial equilibrium when  $2U + W = 0$ . The terms  $U$  and  $W$  are expressed as

$$U = \frac{3M\Delta V^2}{16 \ln 2} \quad (10)$$

and

$$W = -a \frac{GM^2}{R} \left[ 1 - \left( \frac{\Phi}{\Phi_{\text{cr}}} \right)^2 \right], \quad (11)$$

respectively, where the values  $\Phi$  and  $\Phi_{\text{cr}}$  are, respectively, the magnetic flux penetrating the clump and the critical magnetic flux above which the magnetic field can support the clump against the self-gravity. Here, we adopt  $\Phi = 0$  for simplicity, which means no magnetic support. The value  $a$  is a dimensionless parameter of order unity

which measures the effects of a nonuniform or nonspherical mass distribution (Bertoldi & McKee 1992). For a uniform sphere and a centrally-condensed sphere with  $\rho \propto r^{-2}$ ,  $a = 3/5$  and 1, respectively. For the  $\text{HCO}^+$  clump, the effects of the nonspherical mass distribution appear to be small because the aspect ratios are not so far from unity (see also Figure 2 of Bertoldi & McKee 1992). Here, we adopt  $a = 1$  because the clump seems centrally-condensed.

Then, the terms  $U$  and  $W$  are estimated to be  $2U = 270 - 390 \text{ M}_\odot \text{ km}^2 \text{ s}^{-2}$  and  $W = -350 \text{ M}_\odot \text{ km}^2 \text{ s}^{-2}$ , respectively, which yields the virial ratio, the ratio between  $2U$  and  $W$ , of  $0.8 - 1.1$ . This value increases by a factor of about 1.3, if we adopt the magnetic field strength derived by Sugitani et al. (2011). The dense clump as a whole is close to quasi-virial equilibrium. On the other hand, the outflow kinetic energy of the central dense part detected in the CO ( $J = 3 - 2$ ) emission is derived as  $E_{\text{out}} \sim 24 \text{ M}_\odot \text{ km}^2 \text{ s}^{-2}$ , corresponding to about 7 % the global gravitational energy, where we adopted the value corrected for the inclination angle  $\xi = 57.3^\circ$ . Therefore, the energy input due to the current outflows may not contribute to change the global kinetic energy significantly. In other words, the current outflow activity observed in Serpens South appears not to be enough to disperse the whole cluster-forming clump (see also Maury et al. 2009 for the case of NGC2264-C). We note that the terms  $U$  and  $W$  increase with  $D^2$  and  $D^3$ , respectively, and therefore the virial ratio decreases by a factor of 1.6 if we adopt  $D = 410 \text{ pc}$ , instead of  $260 \text{ pc}$ . Since this factor and the factor due to the magnetic support almost cancel each other out, the dense clump is likely to be close to the virial equilibrium.

The presence of Class II YSOs in this region suggests that star formation has lasted over  $10^6$  years, assuming the typical Class II timescale of about  $10^6 \text{ yr}$ . However, the low fraction of Class II relative to Class I sources implies that the ages of the YSOs in this region may be younger than those in other nearby cluster-forming regions (Gutermuth et al. 2009). The age of this region may be  $10^{5-6} \text{ yr}$ . This corresponds to a few  $\sim 20$  free-fall times of the clump assuming the mean density of  $5 \times 10^5 \text{ cm}^{-3}$ , where

$$t_{\text{ff}} = \left( \frac{3\pi}{32G\rho_0} \right)^{1/2}. \quad (12)$$

According to Gutermuth et al. (2008), about 30 Class I and II stars are associated with the area where we detected the strong  $\text{HCO}^+$  emission. Assuming the median stellar mass of  $0.5 \text{ M}_\odot$ , the star formation efficiency in the dense part is derived as about 15 – 20 %, as reasonably high as those of other nearby cluster-forming clumps. This corresponds to about 1 – 5 % of the star formation rate per free-fall time. This value is in good agreement with that estimated by Krumholz & Tan (2007). Since the current outflow activity does not provide enough kinetic energy to destroy the clump, subsequent star formation is expected to continue. This is consistent with the quasi-virial equilibrium model for which cluster formation continues for a few or more free-fall times.

## 5. SUMMARY

We carried out the CO ( $J = 3 - 2$ ) and  $\text{HCO}^+$  ( $J = 4 - 3$ ) observations toward the nearest cluster-forming IRDC, Serpens South, using the ASTE 10 m telescope. The main results are summarized as follows.

1. We found that many outflow components concentrate in the dense part where the protocluster resides. Most of these outflow components appear to move away from the dense part. In the northern part, we identified only three bipolar outflows, indicating that the star formation is less active in the northern part.

2. Most of the outflow components tend to be anti-correlated with the dense gas traced by the 1.1 mm continuum emission. Furthermore, the propagation directions of the outflows are across the global magnetic field direction (Sugitani et al. 2011). A couple of strong red-shifted outflow components appear to interact with the dense gas.

3. The central dense clump detected by the  $\text{HCO}^+$  ( $J = 4 - 3$ ) emission has a mass of  $80 \text{ M}_\odot$  and a radius of about 0.1 pc, with an axis ratio of about 2. The average density and velocity width are estimated at about  $5 \times 10^5 \text{ cm}^{-3}$  and  $2.5 - 3 \text{ km s}^{-1}$ , respectively. The dense clump has very clumpy structures. Some of the subfragments appear to coincide with the positions of the Class 0 candidates identified by Bontemps et al. (2010).

4. We estimated the global physical quantities of the outflows. The total outflow mass, momentum, and energy seem smaller than those of the Serpens Cloud Core, a nearby typical parsec-scale cluster-forming clump, located about  $3^\circ$  north of Serpens South. However, the characteristic outflow speed appears somewhat larger than that of the Serpens Cloud Core. This may imply that the YSO populations of Serpens South are younger than those of the Serpens Cloud Core.

5. The outflow energy injection rate is likely to be somewhat larger than the energy dissipation rate of the supersonic turbulence, suggesting that the outflow feedback can significantly contribute to the generation of the supersonic turbulence in the dense clump. Assuming the median stellar mass of  $0.5 \text{ M}_\odot$ , the mean outflow momentum per unit stellar mass is estimated to be about  $4 \text{ km s}^{-1}$ , under the assumption of optically-thin gas. This mean outflow momentum corresponds to the non-dimensional outflow parameter of  $f \sim 0.04$ , which gauges the strength of a outflow. This value of  $f$  is somewhat smaller than the fiducial values of  $f = 0.4$  adopted by Matzner & McKee (2000), Li & Nakamura (2006), and Nakamura & Li (2007). If we take into account the effect of the optical depth, the outflow strength  $f$  presumably increases by a factor of a few.

6. The total outflow energy appears significantly smaller than the global gravitational energy of the dense part where the protocluster is located. In other words, it may be difficult to destroy the cluster-forming clump by the current outflow activity. This may be inconsistent with the dynamical model of cluster formation, for which the outflow feedback due to the initial star burst is envisioned to disperse the dense gas from the cluster-forming clump.

This work is supported in part by a Grant-in-Aid for Scientific Research of Japan (20403003, 20540228, 22340040) and National Science Council of Taiwan



(Grant No. 98-2112-M-001-002-MY3). We thank Philippe André for helpful comments. We are grateful to the ASTE staffs for both operating the ASTE telescope and helping us with the data reduction. The ASTE project is driven by Nobeyama Radio Observatory (NRO), a branch of National Astronomical Observatory of Japan (NAOJ), in collaboration with University of Chile, and Japanese institutes including University of Tokyo, Nagoya University, Osaka Prefecture University, Ibaraki University, and Hokkaido University. The ob-

servations with ASTE were carried out remotely from Japan by using NTT's GEMnet2 and its partner R&E (Research and Education) networks, which are based on AccessNova collaboration of University of Chile, NTT Laboratories, and National Astronomical Observatory of Japan. This research has made use of the NASA/IPAC Infrared Science Archive, which is operated by the Jet Propulsion Laboratory, California Institute of Technology, under contract with the National Aeronautics and Space Administration.

## REFERENCES

- Allen, L. et al. 2006. in *Protostars and Planets V*, eds. B. Reipurth, D. Jewitt, and K. Keil (The University of Arizona Press), p. 361
- André, P. et al. 2010, *A&A*, 518, L102
- André, P. et al. 2007, *A&A*, 472, 519
- Arce, H. G., Borkin, M. A., Goodman, A. A., Pineda, J. E., & Halle, M. W. 2010, *ApJin press*
- Bertoldi, F., & McKee, C. F. 1992, *ApJ*, 395, 140
- Bontemps, S., André, P., Terebey, S., & Cabrit, S. 1996, *A&A*, 311, 858
- Bontemps, S. et al. 2010, *A&A*, 518, L85
- Boogert, A. C. A., Hogerheijde, M. R., Ceccarelli, C., Tielens, A. G. G. M., van Dishoeck, E. F., Blake, G. A., Latter, W. B., & Motte, F., 2002, *ApJ*, 570, 708
- Butler, M. J., Tan, J. C. 2009, *ApJ*, 696, 484
- Carroll, J. J., Frank, A., & Blackman, E. G. 2010, *ApJ*, 722, 145
- Cabrit, S. & Bertout, C. 1992, *A&A*, 261, 274
- Davis, C. J., Matthews, H. E., Ray, T. P., Dent, W. R. F., & Richer, J. S. *MNRAS*, 309, 141
- Dzib, S. et al. 2010, *ApJ*, 718, 610
- Ezawa, H., Kawabe, R., Kohno, K., & Yamamoto, S. 2004, *Proc. SPIE*, 5489, 763
- Elmegreen, B. G. 2007, *ApJ*, 668, 1064
- Graves, S. F., et al. 2010, *ApJ*, in press (arXiv:1006.0891)
- Gorlova, N., Steinhauer, A., & Lada, E. 2010, *ApJ*, 716, 634
- Gutermuth, R. A. et al. *ApJ*, 2008, 673, L151
- Gutermuth, R. A. et al. *ApJS*, 2009,
- Gutermuth, R. A. et al. 2011, submitted to *ApJ*
- Hartmann, L., & Burkert, A. 2007, *ApJ*, 654, 988
- Kamazaki, T., Saito, M., Hirano, N., Umemoto, T. & Kawabe, R. *ApJ*, 2003, 584, 357
- Kirk, H. et al. 2007, *ApJ*, 668, 1042
- Krumholz, M. R., Matzner, C. D., McKee, C. F. 2006, *ApJ*, 653, 361
- Krumholz, M. R. & Tan, J. C. 2007, *ApJ*, 656, 959
- Klessen, R. S. & Hennebelle, P. 2010, *A&A*, 520, 17
- Lada, C. J. & Lada, E. A. *ARA&A*, 2003, 41, 57
- Li, Z.-Y. & Nakamura, F. *ApJ*, 2006, 640, L187
- Li, Z.-Y., Wang, P., Abel, T., & Nakamura, F. *ApJ*, 2010, 720, L26
- Mac Low, M.-M. 1999, *ApJ*, 524, 169
- Maruta, H., Nakamura, F., Nishi, R., Ikeda, N., & Kitamura, Y. 2010, *ApJ*, 714, 680
- Matzner, C. D., & McKee, C. F. 2000, *ApJ*, 545, 364
- Matzner, C. D. *ApJ*, 2007, 659, 1394
- Maury A., André, P., & Li, Z.-Y. *ApJ*, 2009, 499, 175
- McKee, C. F., & Ostriker, E. C. 2007, *ARA&A*, 45, 565
- Myers, P. C. 2009, *ApJ*, 700, 1609
- Nakamura, F. & Li, Z.-Y. 2007, *ApJ*, 662, 395
- Nakamura, F. & Li, Z.-Y. 2011, submitted to *ApJ*
- Nakamura, F. et al. 2011, *ApJ*, 726, 46
- Noriega-Crespo, A., Moro-Martin, A., Carey, S., Morris, P. W., Padgett, D. L., Latter, William B., & Muzerolle, J. 2004, *ApJS*, 154, 402
- Norman, C., & Silk, J. 1980, *ApJ*, 238, 158
- Peters, T., Klessen, R. S., Mac Low, M.-M., Banerjee, R., 2010, *ApJ*, 725, 134
- Perreto, N. et al. 2006, *A&A*, 445, 979
- Perreto, N. & Fuller, G. A. 2009, *A&A*, 505, 405
- Rathborne, J. M., Jackson, J. M., Simon, R. 2006, *A&A*, 641, 389
- Ridge, N. A., Wilson, T. L., Megeath, S. T., Allen, L. E., & Myers, P. C. 2003, *AJ*, 126, 286
- Rodney, S. A. & Reipurth, B. 2008, in *Handbook of Star Forming Regions Vol. II*, Astronomical Society of the Pacific, eds. Bo Reipurth
- Saito, H., Saito, M., Yonekura, Y., & Nakamura, F. 2008, *ApJS*, 178, 302
- Sandell, G. & Knee, L. B. G. 2001, *ApJ*, 546, L49
- Schneider, N., Csengeri, T., Bontemps, S., Motte, F., Simon, R., Hennebelle, P., Federrath, C., & Klessen, R. *A&A*, 2010, 520, 49
- Stone, J. M., Ostriker, E. C., & Gammie, C. F. 1998, *ApJ*, 508, L99
- Straizys, V., Cernis, K., & Bartasiute, S. 1996, *Baltic Astron.*, 5, 125
- Sugitani, K. et al. 2010, *ApJ*, 716, 299
- Sugitani, K. et al. 2011, *ApJ*, in press (arXiv:1104.2977)
- Takami, M., Karr, J. L., Koh, H., Chen, H.-H., & Lee, H.-T. *ApJ*, 2010, *ApJ*, 720, 155
- Tan, J. C., Krumholz, M. R., & McKee, C. F. 2006, *ApJ*, 641, L121
- Vazquez-Semadeni, E., Colin, P., Gomez, G. C., Ballesteros-Paredes, J., Watson, A. W. 2010, *ApJ*, 715, 1302
- Walsh, A. J., Myers, P. C., Di Francesco, J., Mohanty, S., Bourke, T. L., Gutermuth, R., Wilner, D. 2007, *ApJ*, 655, 958
- Wang, P., Li, Z.-Y., Abel, T., & Nakamura, F. 2010, *ApJ*, 709, 27
- Wilson, G. W., et al. 2008, *MNRAS*, 386, 807
- Winston, E. et al. 2010, *AJ*, 140, 266
- Zhang, M. & Wang, H. 2009, *AJ*, 138, 1830

TABLE 1  
CHARACTERISTICS OF IDENTIFIED CO ( $J = 3 - 2$ ) OUTFLOW LOBES

Name	counterpart <sup>a</sup>	driving source <sup>b</sup>	features
B1	unknown	source 1	central part
B2	unknown	unknown	central part
B3	unknown	unknown	central part
B4	R2, R3	source 2	central part, strong
B5	unknown	source 4	central part, related to R4
B6	unknown	source 3	central part
B7	no	unknown	southern part
B8	R2, R3 ?	source 2 ?	central part, a head of B4 ?
B9	unknown	source 3 ?	a head of B6 ?, outflow or infall gas
B10	R5	unknown	northern part, clear bipolar
B11	R6	unknown	northern part, clear bipolar
B12	R7	unknown	northern part, clear bipolar
B13	no	unknown	eastern part
B14	no	source 5	southern part
B15	R8	source 6	southern part, clear bipolar
B16	R10	Herschel source	northern part, clear bipolar
R1	unknown	source 1	central part
R2	B4	source 2	central part, strong
R3	B4	source 2	central part, strong
R4	unknown	source 4	central part, related to B5
R5	B10	unknown	northern part, clear bipolar
R6	B11	unknown	northern part, clear bipolar
R7	B12	unknown	northern part, clear bipolar
R8	B15	source 6	southern part, clear bipolar
R9	no	unknown	northern part,
R10	B16	Herschel source	northern part, clear bipolar

NOTE. — See Section 3.2 in detail.

<sup>a</sup> Possible counterparts are indicated. “no” means that only one component is seen.

<sup>b</sup> Possible driving sources are indicated. Sources 1 through 6 are indicated in Figs. 11 and 12.

TABLE 2  
GLOBAL OUTFLOW PROPERTIES DERIVED FROM CO ( $J = 3 - 2$ )

	Mass ( $M_{\odot}$ )	Momentum ( $M_{\odot} \text{ km s}^{-1}$ )	Energy ( $M_{\odot} \text{ km}^2 \text{ s}^{-2}$ )	$V_{\text{out}}$ (km s <sup>-1</sup> )
Blue	0.34	3.7	25.9	10.9
Red	0.27	3.9	38.7	14.4
Total	0.61	7.6	64.6	12.5

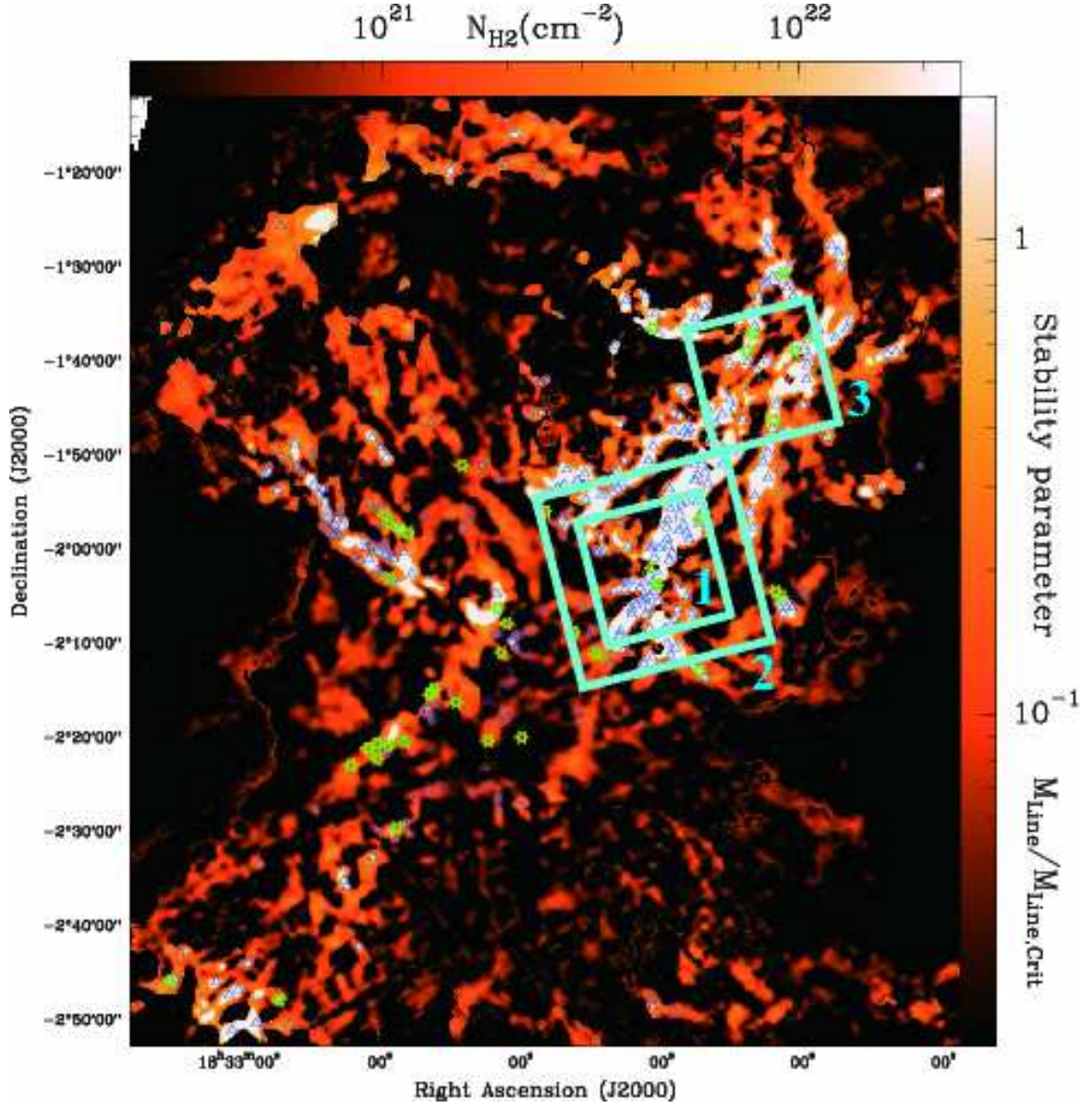


FIG. 1.— Our observation area overlaid on the column density map derived from the Herschel observations. The image is taken from the left panel of Fig. 1 of André et al. (2010), in which the contrast of the filaments was enhanced by a curvelet transform (see the Appendix of André et al. 2010). The blue triangles and green stars indicate the prestellar cores and candidate Class 0 protostars identified with Herschel, respectively. Our observation area is indicated in cyan boxes that are labeled in numbers.

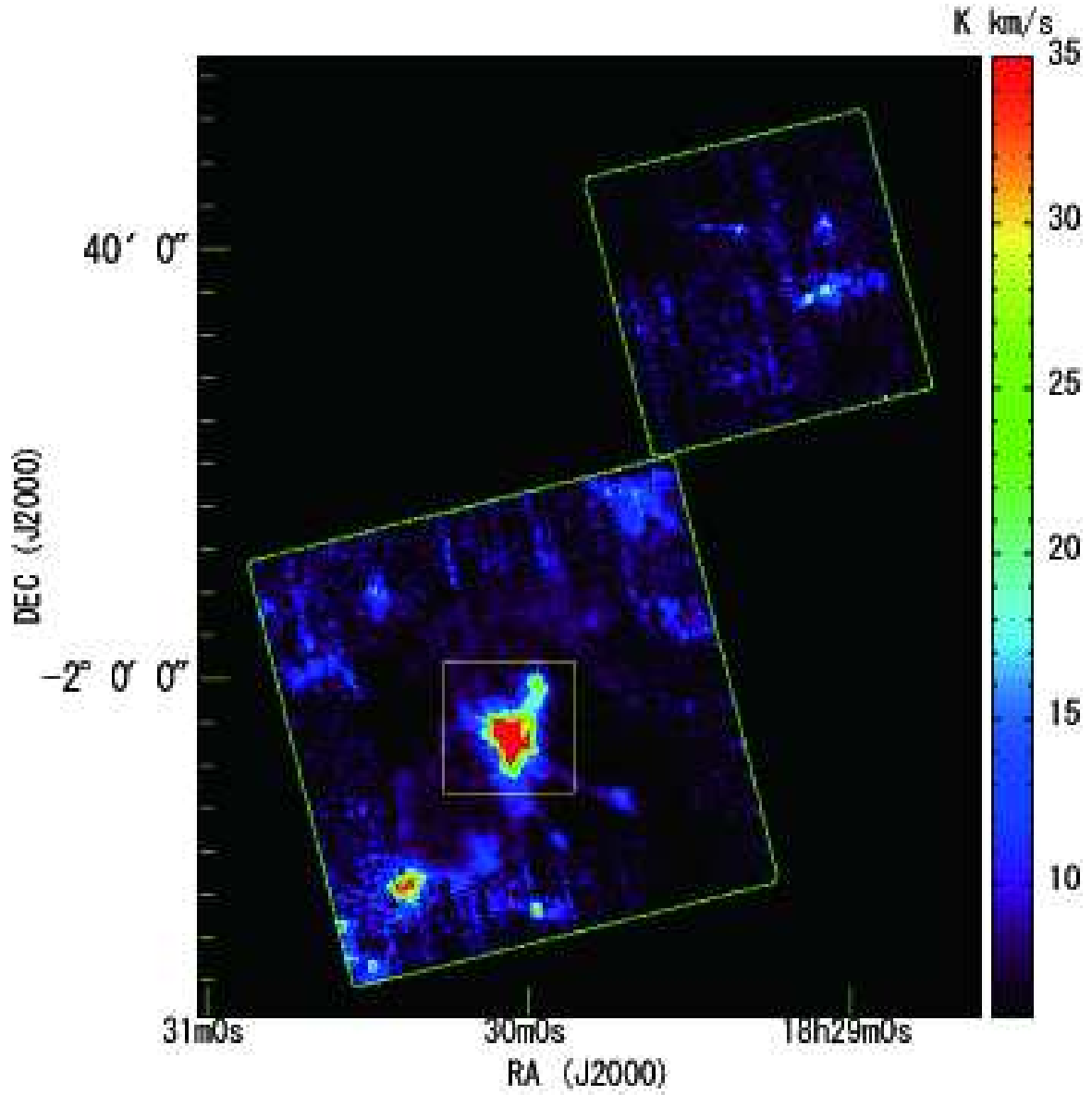


FIG. 2.— CO ( $J=3-2$ ) total integrated intensity map toward Serpens South in the velocity range from  $v_{\text{LSR}} = -2 \text{ km s}^{-1}$  to  $+15 \text{ km s}^{-1}$ . The blow-up of the yellow box is presented in the upper panel of Fig. 6.

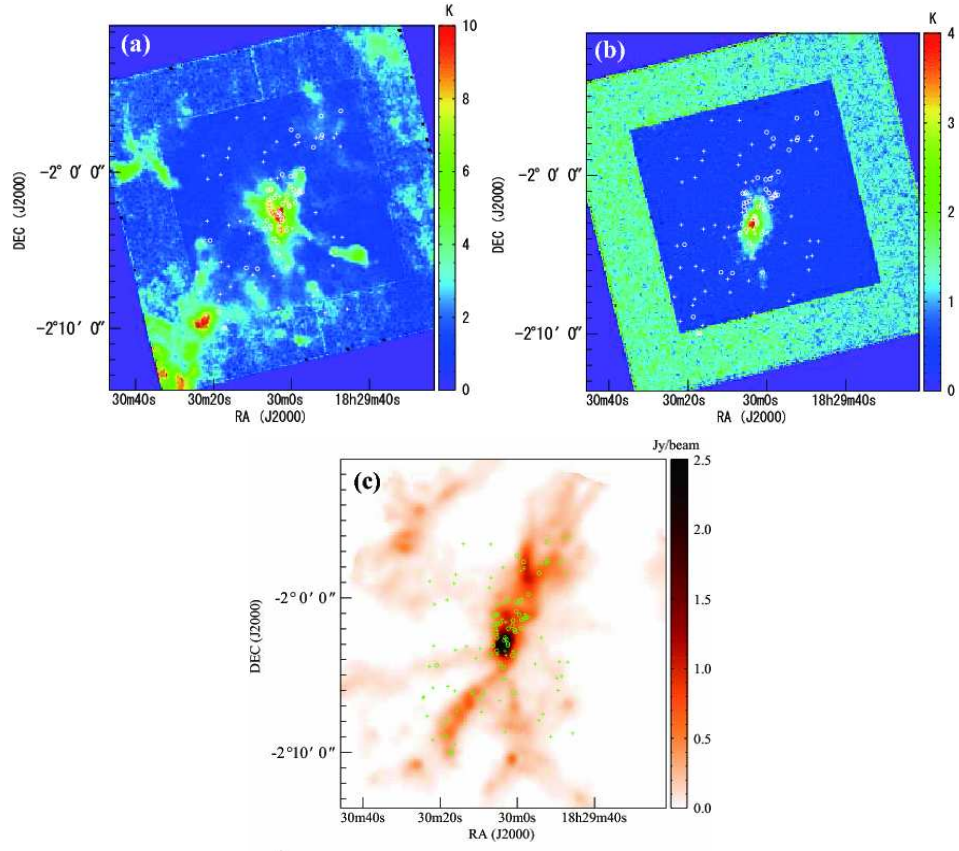


FIG. 3.— (a) CO ( $J = 3 - 2$ ) peak intensity map toward the Serpens South protocluster. (b) HCO<sup>+</sup> ( $J = 4 - 3$ ) peak intensity map toward the same area presented in panel (a). (c) 1.1 mm continuum emission map toward the same area presented in panel (a). The detail of the image will be described in Gutermuth et al. (2011). For all the panels, the circles and crosses indicate the Class I and Class II sources, respectively, identified by Gutermuth et al. (2008).

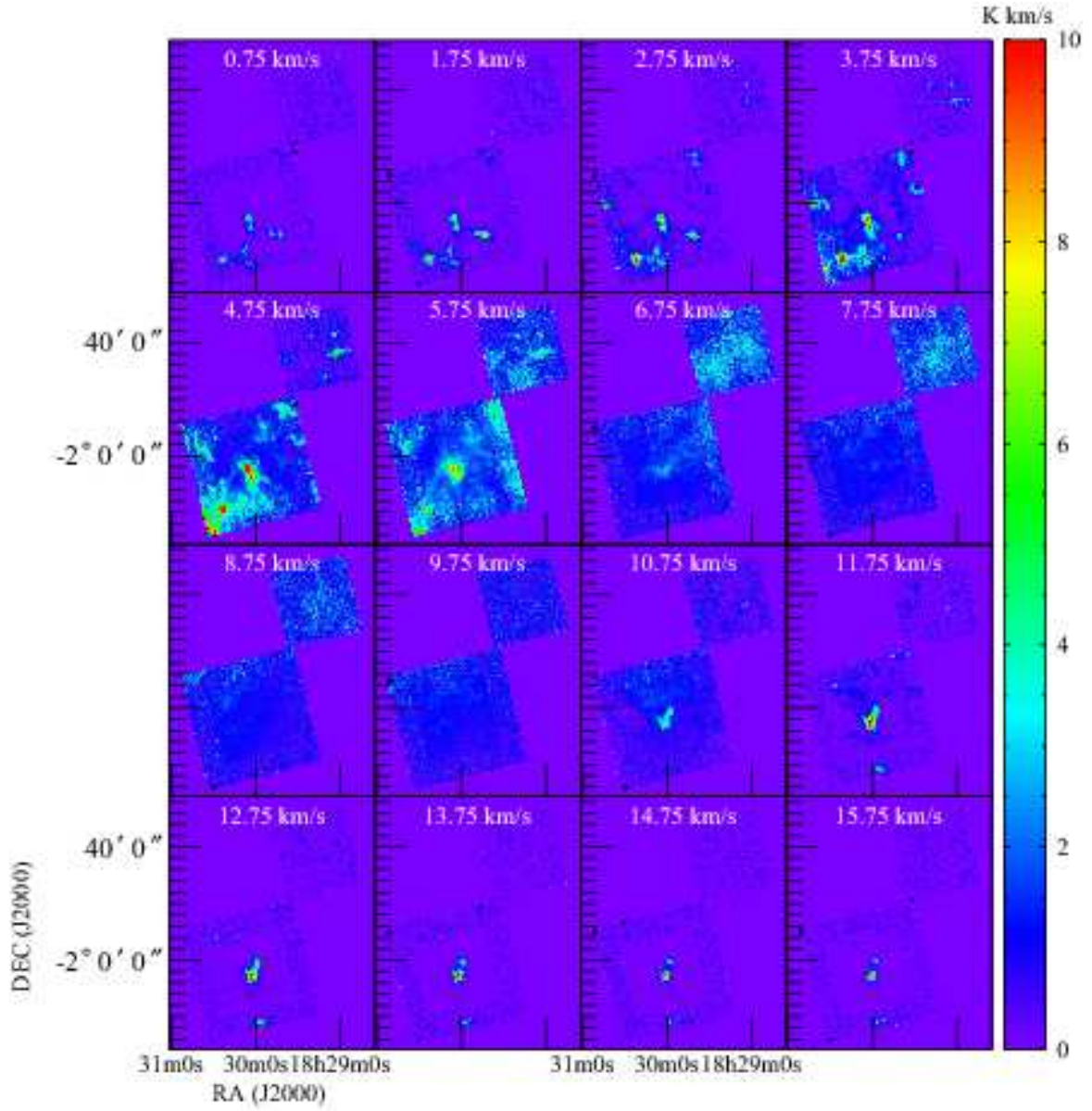


FIG. 4.— Velocity channel maps of the CO ( $J=3-2$ ) emission with the velocity intervals of  $1 \text{ km s}^{-1}$ . The LSR velocity is indicated at the top of each panel.



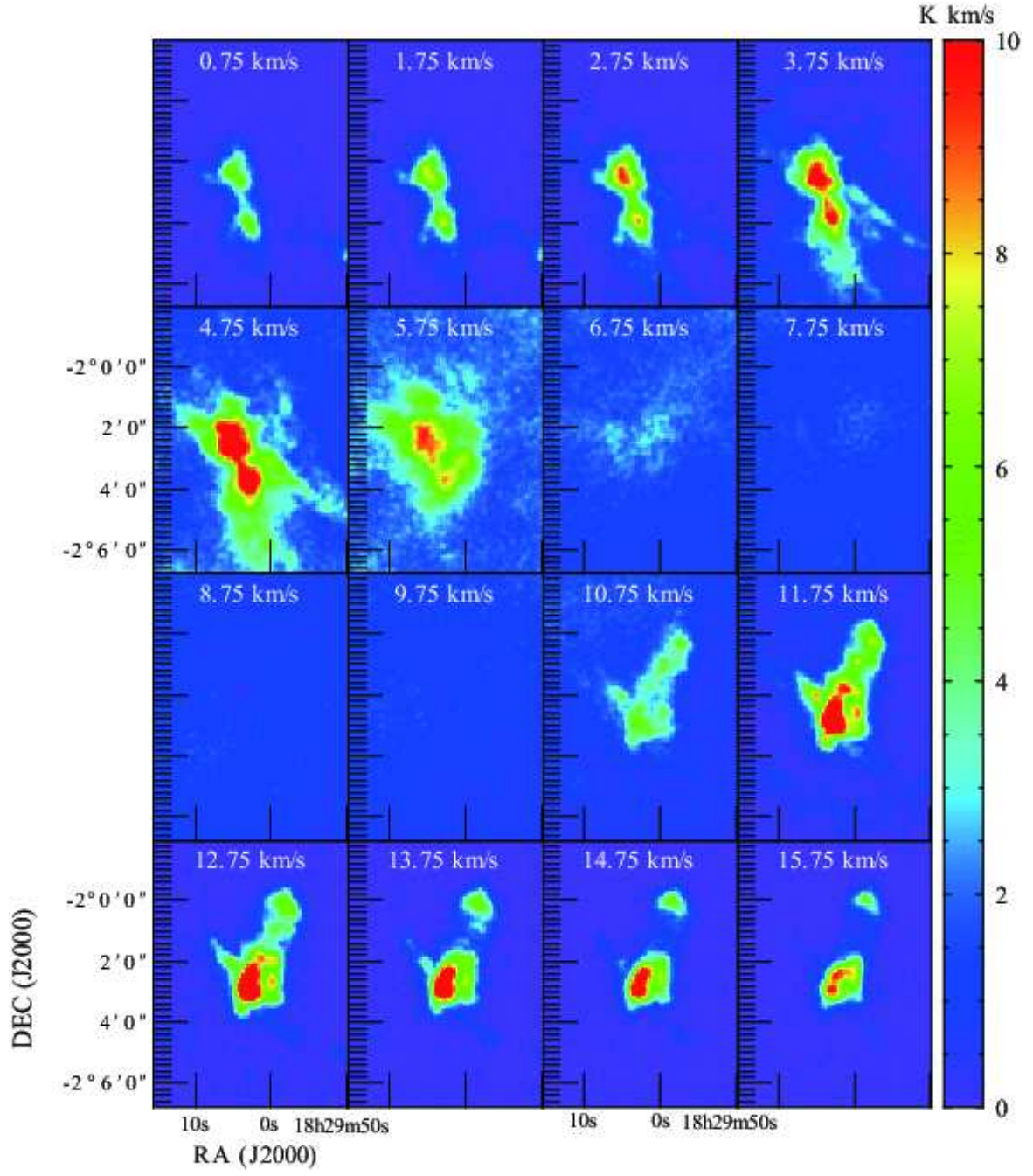


FIG. 5.— Same as Fig. 4 but toward the central region of Serpens South.

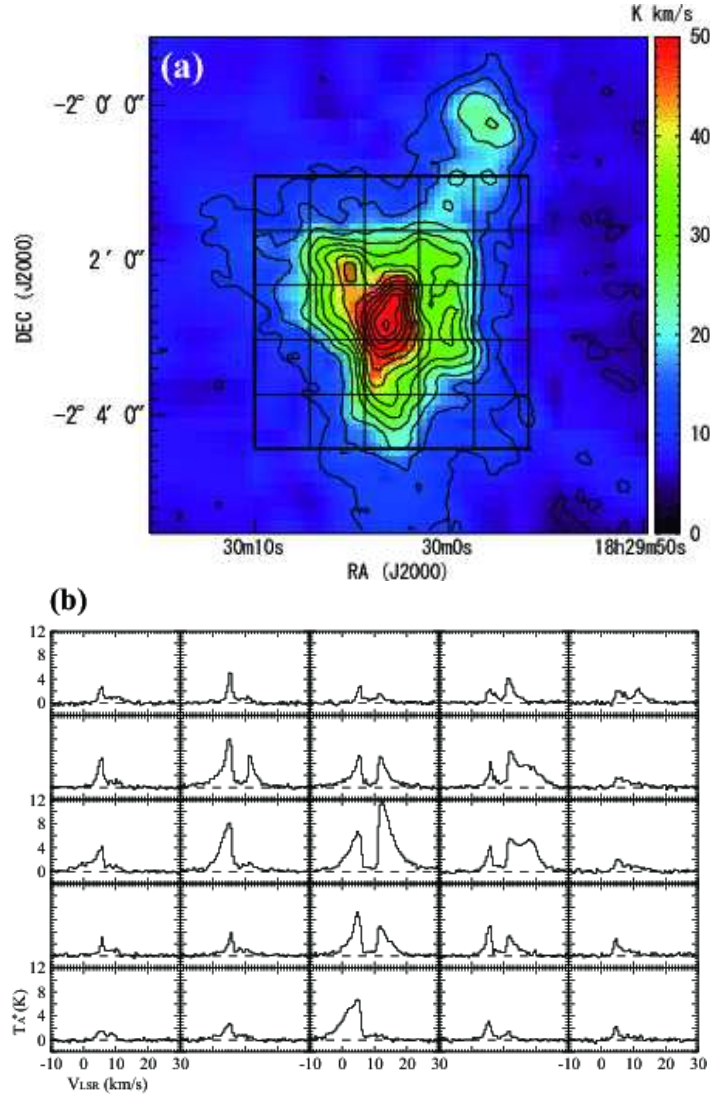


FIG. 6.— *upper panel*: CO ( $J = 3 - 2$ ) total integrated intensity map in the velocity range from  $v_{\text{LSR}} = -2 \text{ km s}^{-1}$  to  $+15 \text{ km s}^{-1}$  toward the yellow box indicated in Fig. 2. The CO ( $J = 3 - 2$ ) integrated intensity is shown in color in units of  $\text{K km s}^{-1}$ . The contours start at  $5 \text{ K km s}^{-1}$  at an interval of  $5 \text{ K km s}^{-1}$ . The boxes indicate the areas where CO ( $J = 3 - 2$ ) spectra take average (see the lower panel of Figure 6). *lower panel*: CO ( $J = 3 - 2$ ) spectra. Each profile is averaged inside each box indicated in Figure 6a.



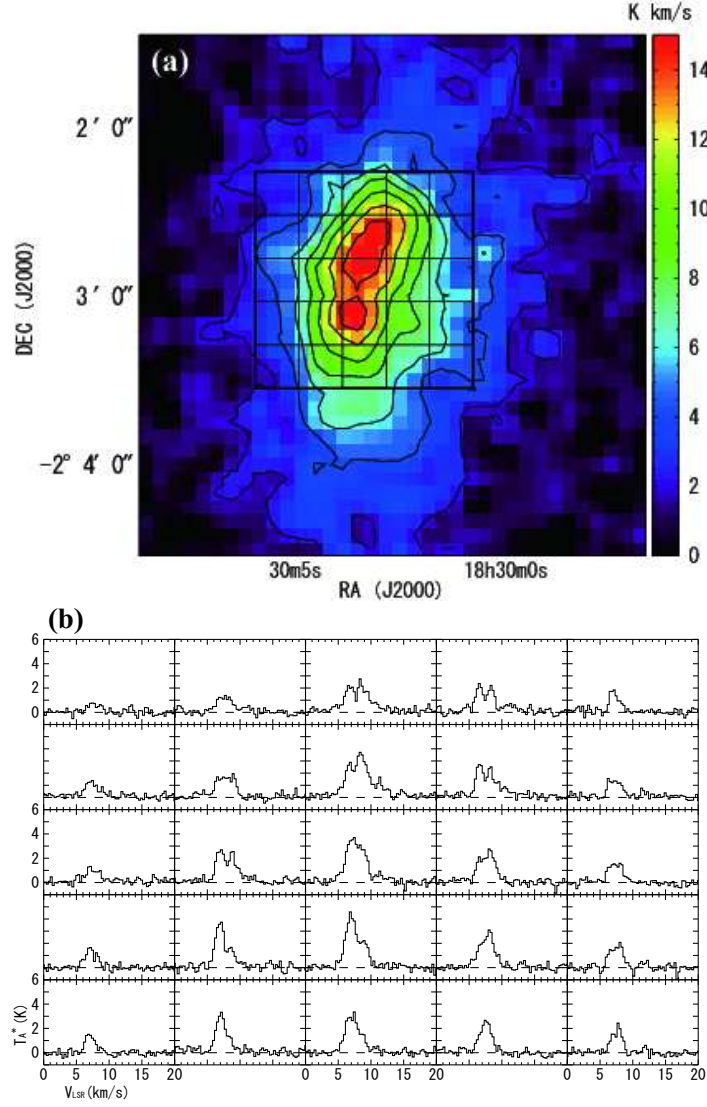


FIG. 7.— *upper panel*:  $\text{HCO}^+$  ( $J=4-3$ ) total integrated intensity map in the velocity range from  $v_{\text{LSR}} = 2.25 \text{ km s}^{-1}$  to  $+15.25 \text{ km s}^{-1}$  toward the Serpens South protocluster. The  $\text{HCO}^+$  ( $J=4-3$ ) integrated intensity is shown in color in units of  $\text{K km s}^{-1}$ . The contours start at  $2 \text{ K km s}^{-1}$  at an interval of  $2 \text{ K km s}^{-1}$ . *lower panel*:  $\text{HCO}^+$  ( $J=4-3$ ) spectra. Each profile is averaged inside each box indicated in Figure 7.

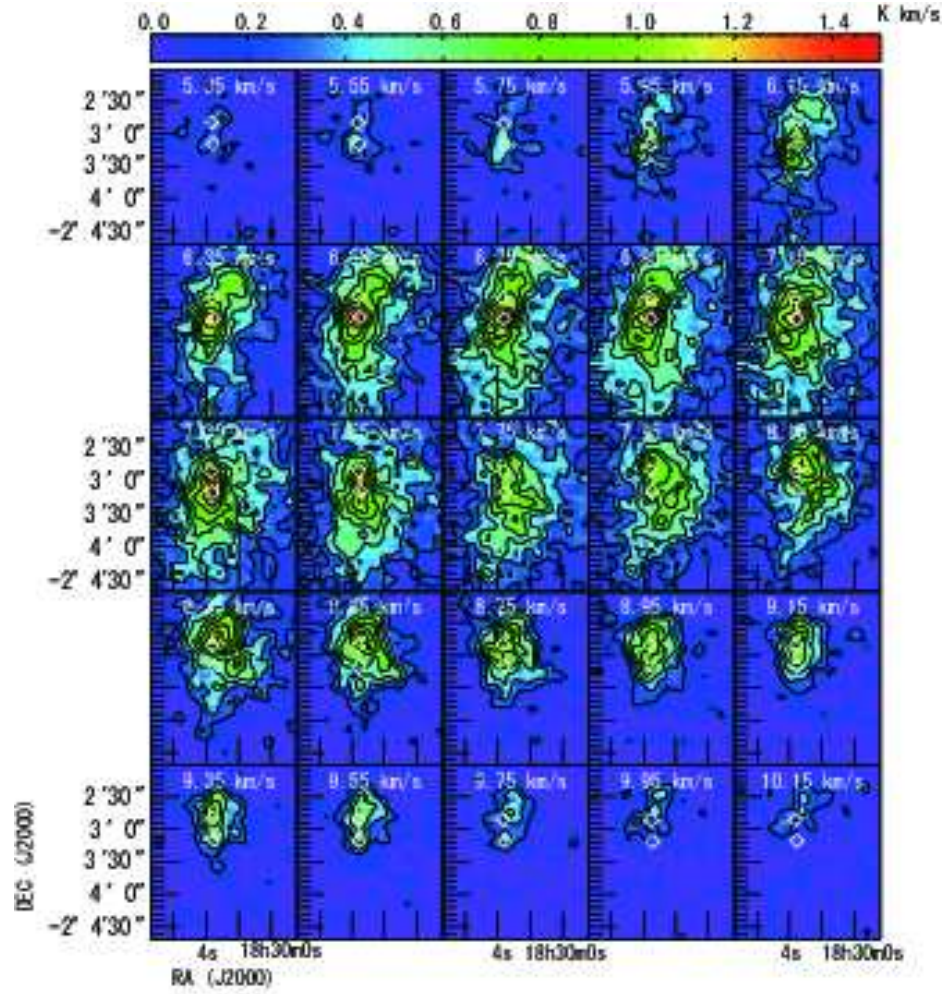


FIG. 8.— Velocity channel maps of the  $\text{HCO}^+$  ( $J = 4 - 3$ ) emission with the velocity intervals of  $0.2 \text{ km s}^{-1}$ . The LSR velocity is indicated at the top of each panel. The contour levels go up in  $0.15 \text{ K km s}^{-1}$  step, starting from  $0.2 \text{ K km s}^{-1}$ . The  $\text{HCO}^+$  ( $J = 4 - 3$ ) channel maps indicate that the dense clump has clumpy structure. The positions of the possible driving sources of the outflows are indicated by the white diamonds (sources 1 and 2 in Fig. 11b). Sources 1 and 2 are the possible driving sources of the R1 and R3 (and R2) outflow lobes, respectively. The latter coincides with the position of the  $1.1 \text{ mm}$  peak (see Section 3.2 in detail).

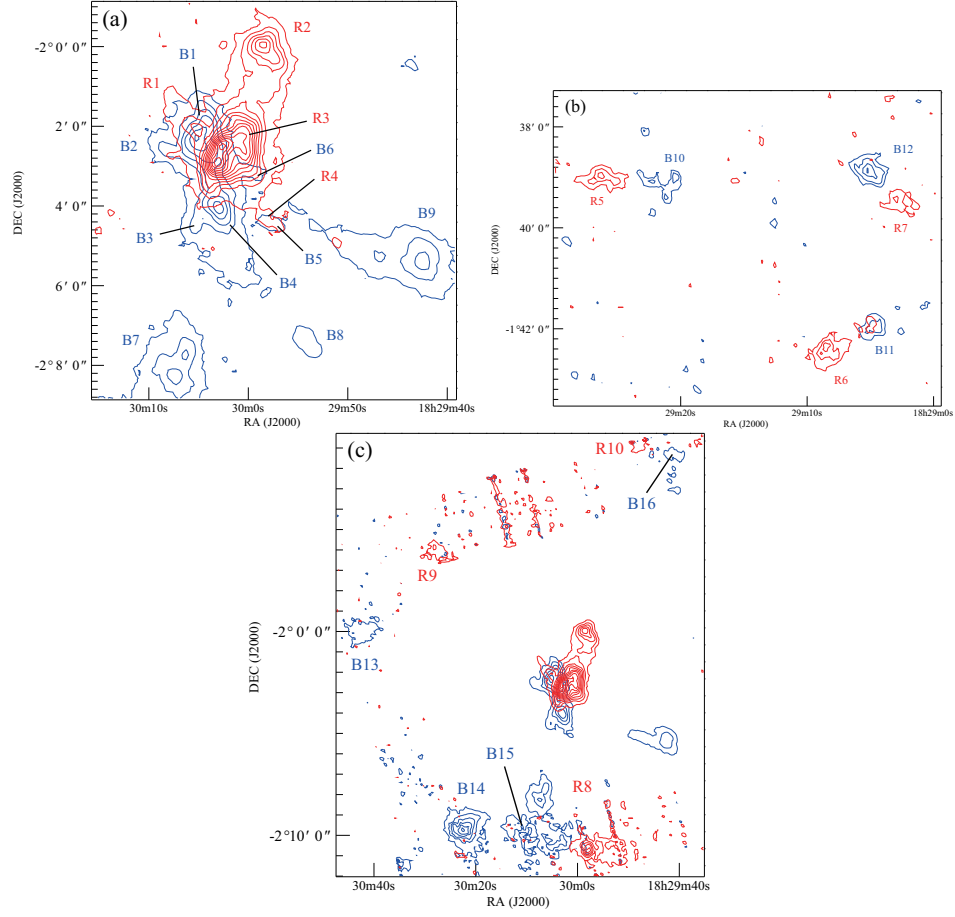


FIG. 9.— (a) Molecular outflow lobes identified from CO ( $J=3-2$ ) emission toward the Serpens South protocluster (Box 1). The blue contours represent blueshifted  $^{12}\text{CO}$  gas and red contours represent redshifted  $^{12}\text{CO}$  gas. The blue and red contour levels go up in  $6 \text{ K km s}^{-1}$  step, starting from  $3 \text{ K km s}^{-1}$ . The integration ranges are  $-9.75$  to  $3.75 \text{ km s}^{-1}$  for blueshifted gas and  $11.25$  to  $29.25 \text{ km s}^{-1}$  for redshifted gas. (b) Same as panel (a) but for the northern part of the Serpens South filament (Box 3). The blue and red contour levels go up in  $6 \text{ K km s}^{-1}$  step, starting from  $6 \text{ K km s}^{-1}$ . (c) Same as panel (a) but for the southern part of the Serpens South filament (Box 2). The blue and red contour levels go up in  $6 \text{ K km s}^{-1}$  step, starting from  $6 \text{ K km s}^{-1}$ .



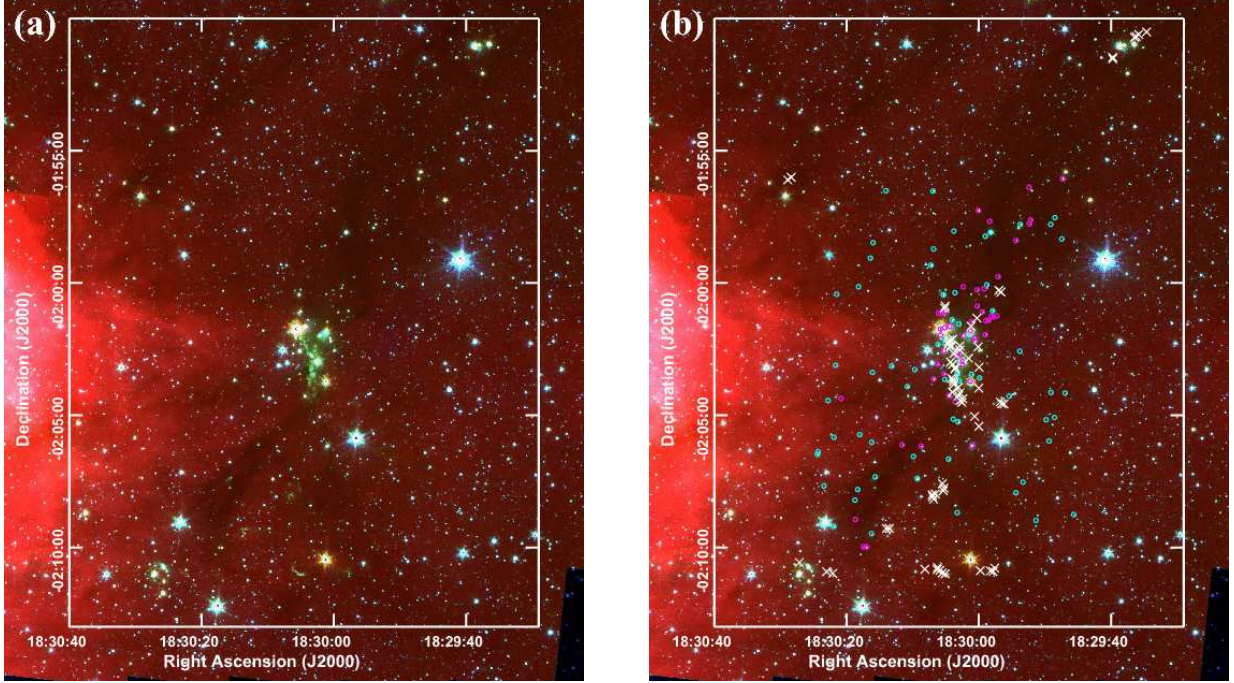


FIG. 10.— (a) Three-color image of Serpens South with IRAC band 1 ( $3.6\ \mu\text{m}$ , blue), IRAC band 2 ( $4.5\ \mu\text{m}$ , green), and IRAC band 4 ( $8.0\ \mu\text{m}$ , red). (b) Same as panel (a) but the positions of Class I (magenta circle) and II (cyan circle) sources identified by Gutermuth et al. (2008) are overlaid. The positions of the infrared H-H objects are indicated by the crosses.

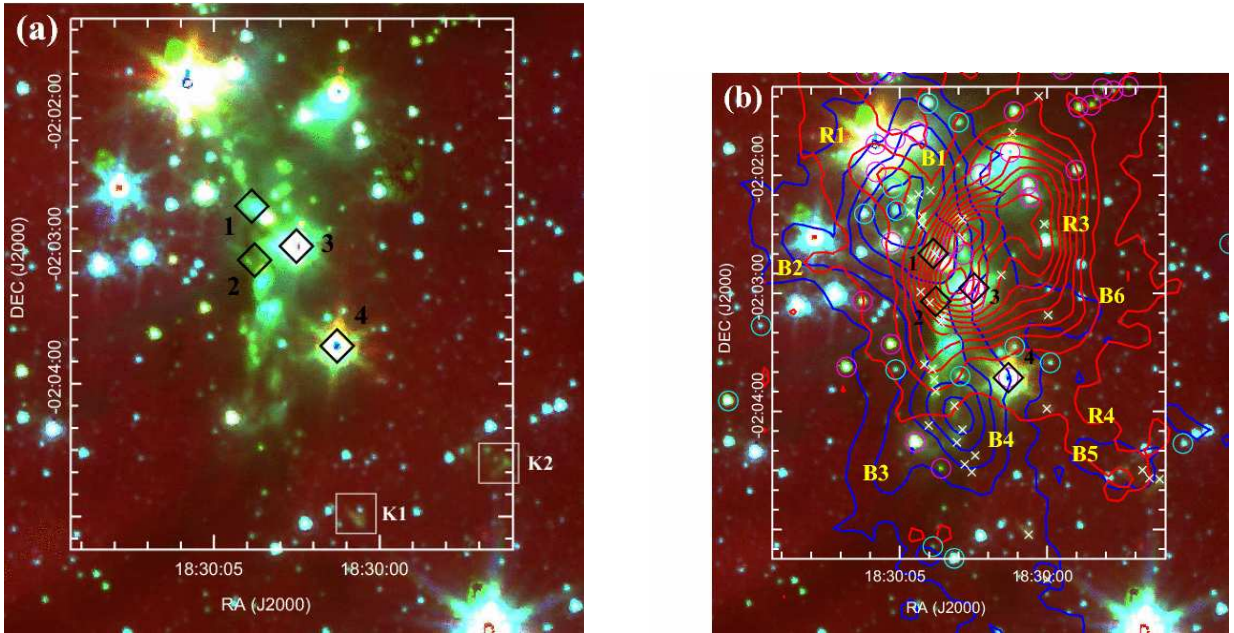


FIG. 11.— (a) Blow-up of the Spitzer IRAC image toward the central region of Serpens South. The diamonds indicate the positions of the possible outflow driving sources (see Section 3.2 in detail). (b) Same as panel (a) but the blueshifted and redshifted CO ( $J = 3 - 2$ ) outflow lobes are overlaid on the image by the blue and red contours. The contours and circles are the same as those of Fig. 9a and Fig. 10, respectively.

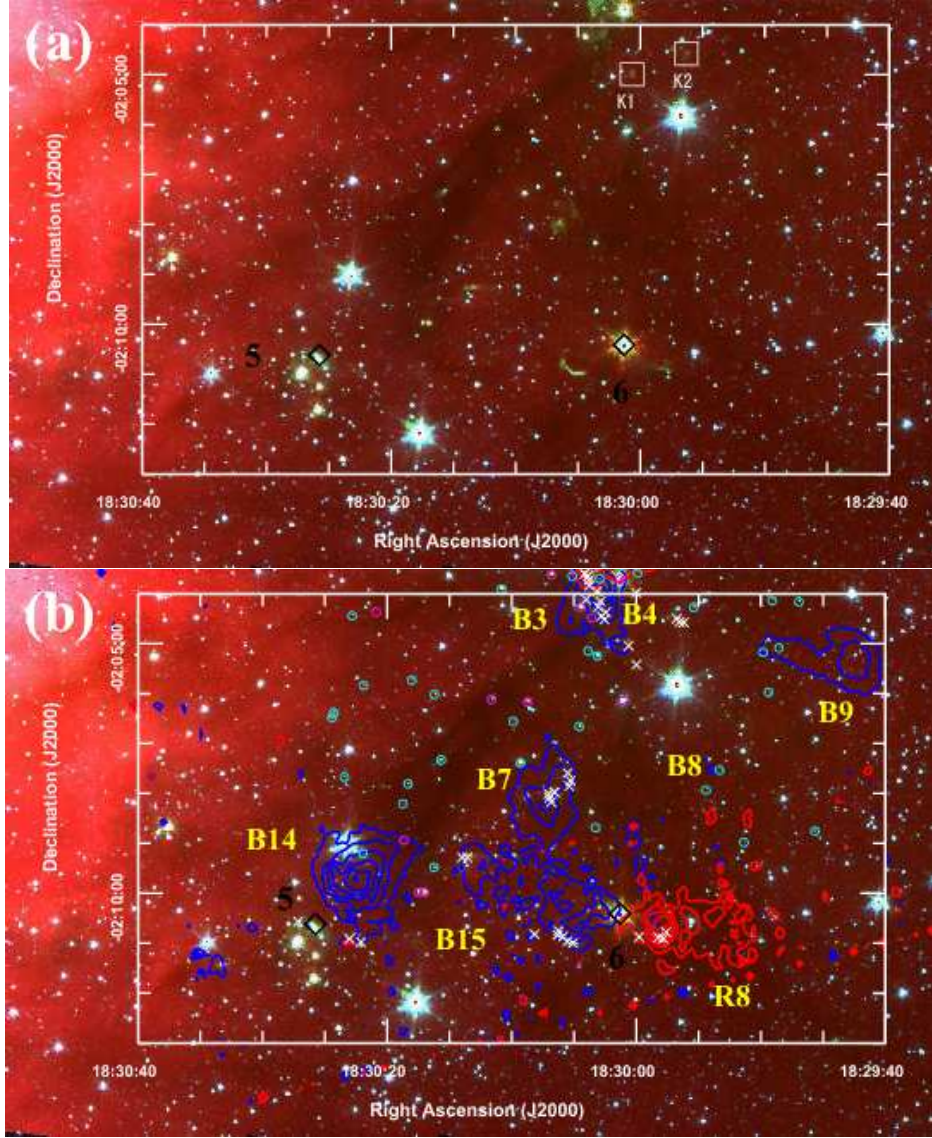


FIG. 12.— (a) Blow-up of the Spitzer IRAC image toward the southern part of Serpens South. The squares indicate the positions of the same objects shown in Fig. 15a. The blow-ups of the areas labeled by K1 and K2 are presented in Fig. 13. (b) Same as panel (a) but the blueshifted and redshifted CO ( $J = 3 - 2$ ) outflow lobes are overlaid on the image by the blue and red contours. The circles and crosses are the same as those of Fig. 10.



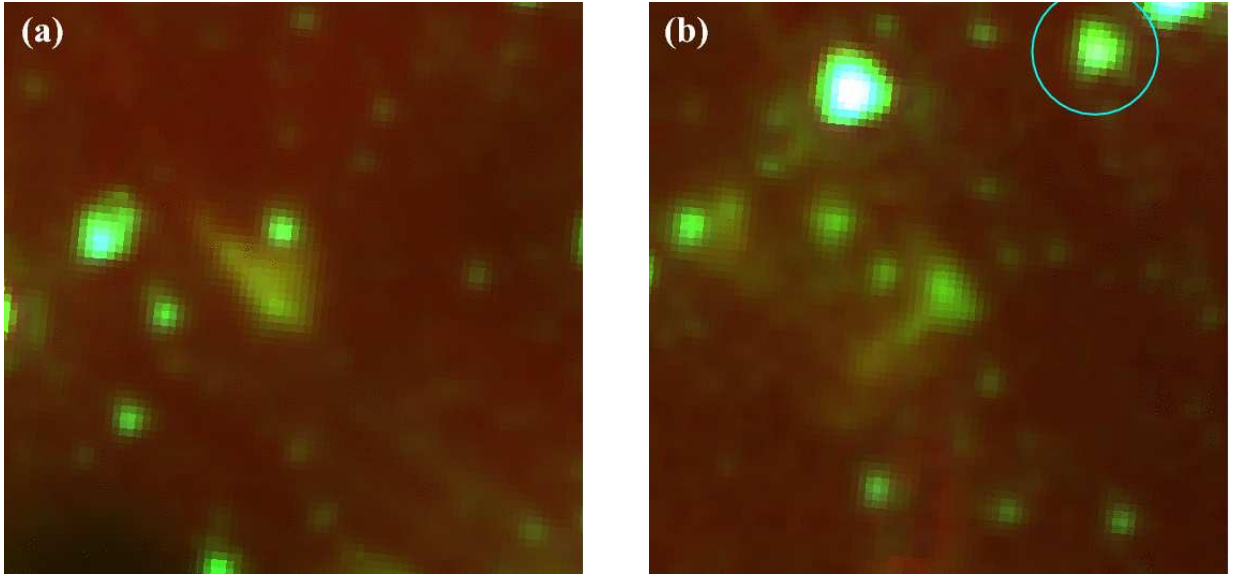


FIG. 13.— Blow-ups of the areas indicated by K1 and K2 in Figs. 11a and 12a. An infrared H-H object having a bow shape is seen near the center of each panel.

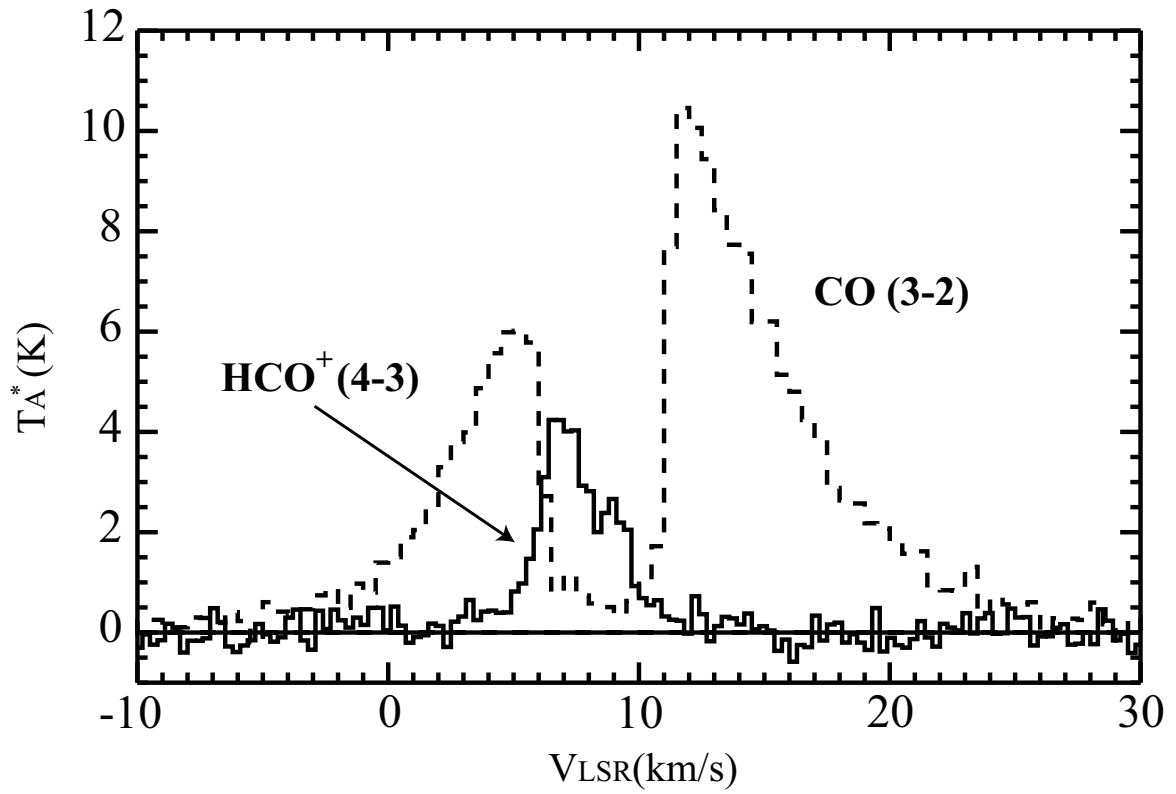


FIG. 14.—  $\text{HCO}^+$  ( $J = 4 - 3$ ) and  $\text{CO}$  ( $J = 3 - 2$ ) line profiles toward source 2 indicated in Fig. 11b. The  $\text{HCO}^+$  ( $J = 4 - 3$ ) shows a clear blue-skewed profile, indicating that the envelope gas is infalling toward the central object.

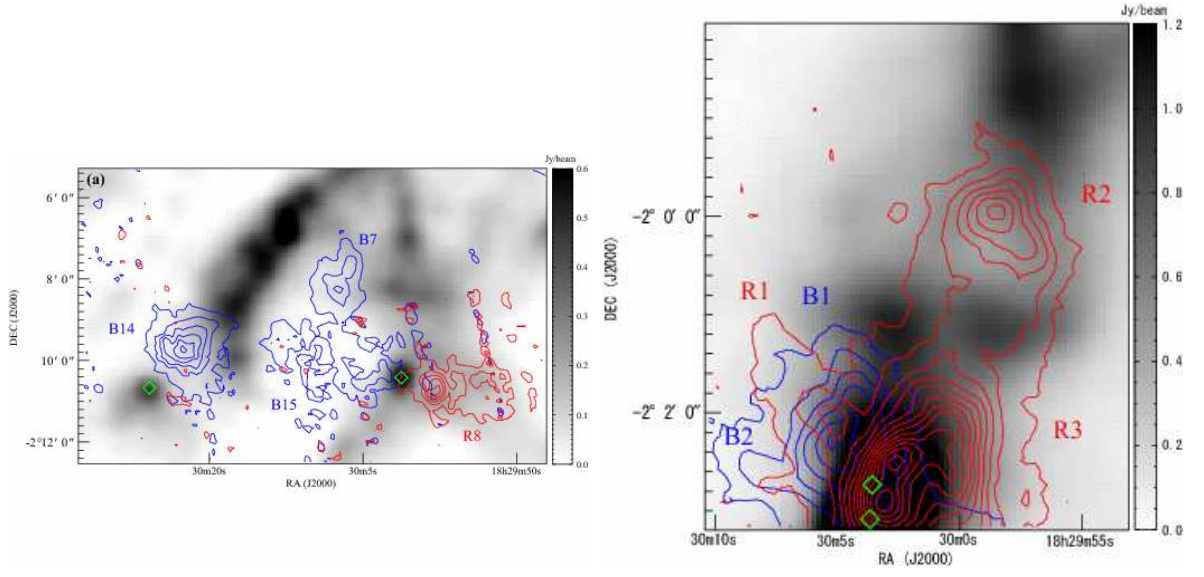


FIG. 15.— (a) Blow-up of the CO ( $J=3-2$ ) outflow lobes located at the southern part of Box 2. The gray colors indicate the 1.1 mm continuum image. The upper and lower diamonds are the possible driving sources of R1 and R3 (and R2), respectively. The latter coincides with the position of the 1.1 mm peak. (b) Same as panel (a) but for the northern part of Box 1. The possible driving sources of the outflows are indicated by the green circles whose positions are determined from the positions of the sources seen in the Spitzer IRAC image. In panels (a) and (b), the blue contours, red contours, and labels are the same as those of Fig. 9.

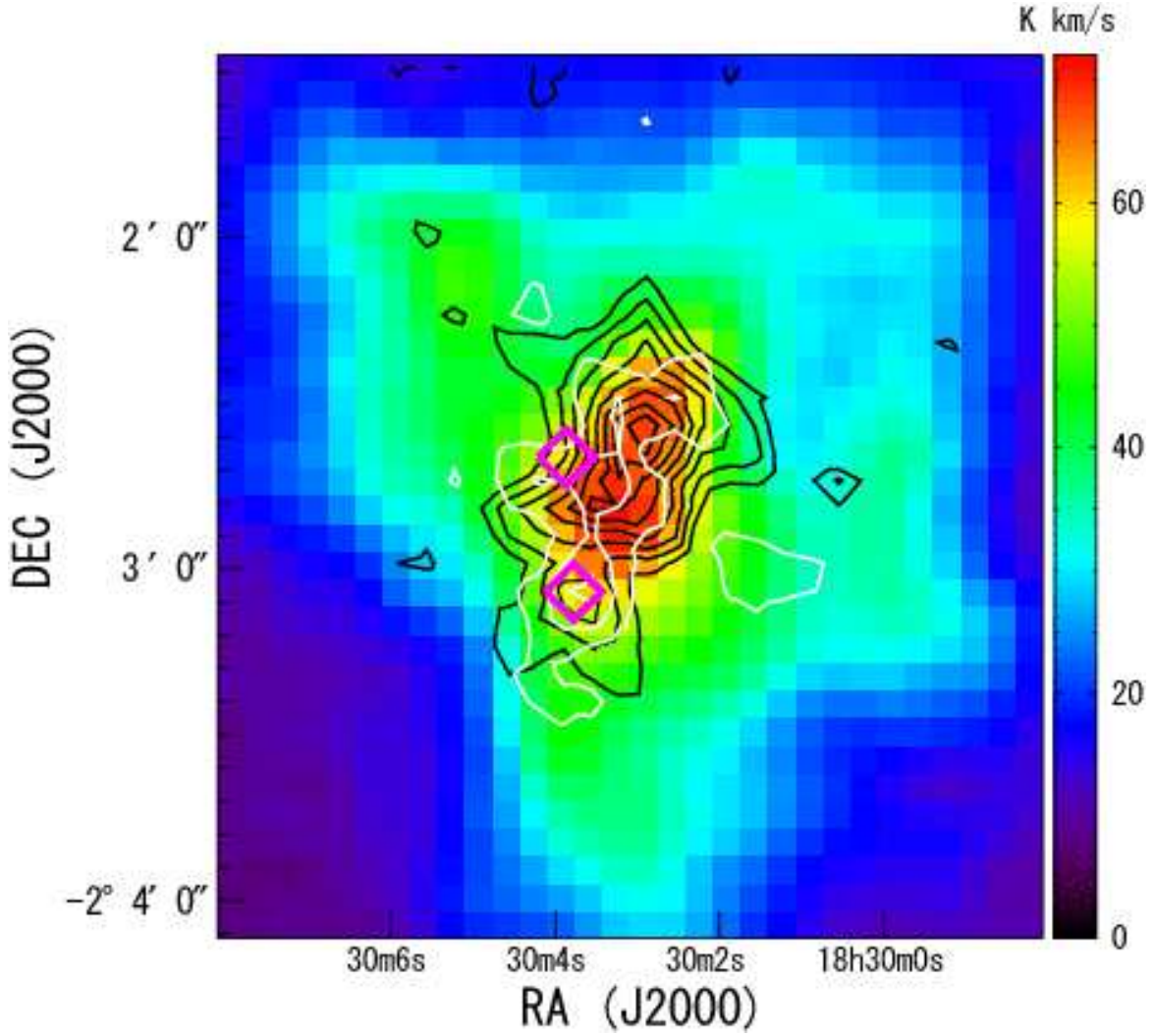


FIG. 16.— High velocity components identified from  $\text{HCO}^+$  ( $J = 4-3$ ) emission toward the Serpens South protocluster. The color image indicates the CO ( $J = 3-2$ ) integrated intensity map in the range of  $2 \text{ km s}^{-1}$  to  $15 \text{ km s}^{-1}$ . The white and black contours represent blueshifted and redshifted gas detected by  $\text{HCO}^+$  ( $J = 4-3$ ), respectively. The white and black contour levels go up in  $0.5 \text{ K km s}^{-1}$  and  $1.0 \text{ K km s}^{-1}$  steps, starting from  $1.0 \text{ K km s}^{-1}$  and  $1.0 \text{ K km s}^{-1}$ , respectively. The integration ranges are  $3.25$  to  $5.75 \text{ km s}^{-1}$  for the blueshifted gas and  $9.75$  to  $15.25 \text{ km s}^{-1}$  for the redshifted gas. The squares indicate the positions of the same objects shown in Fig. 15b.



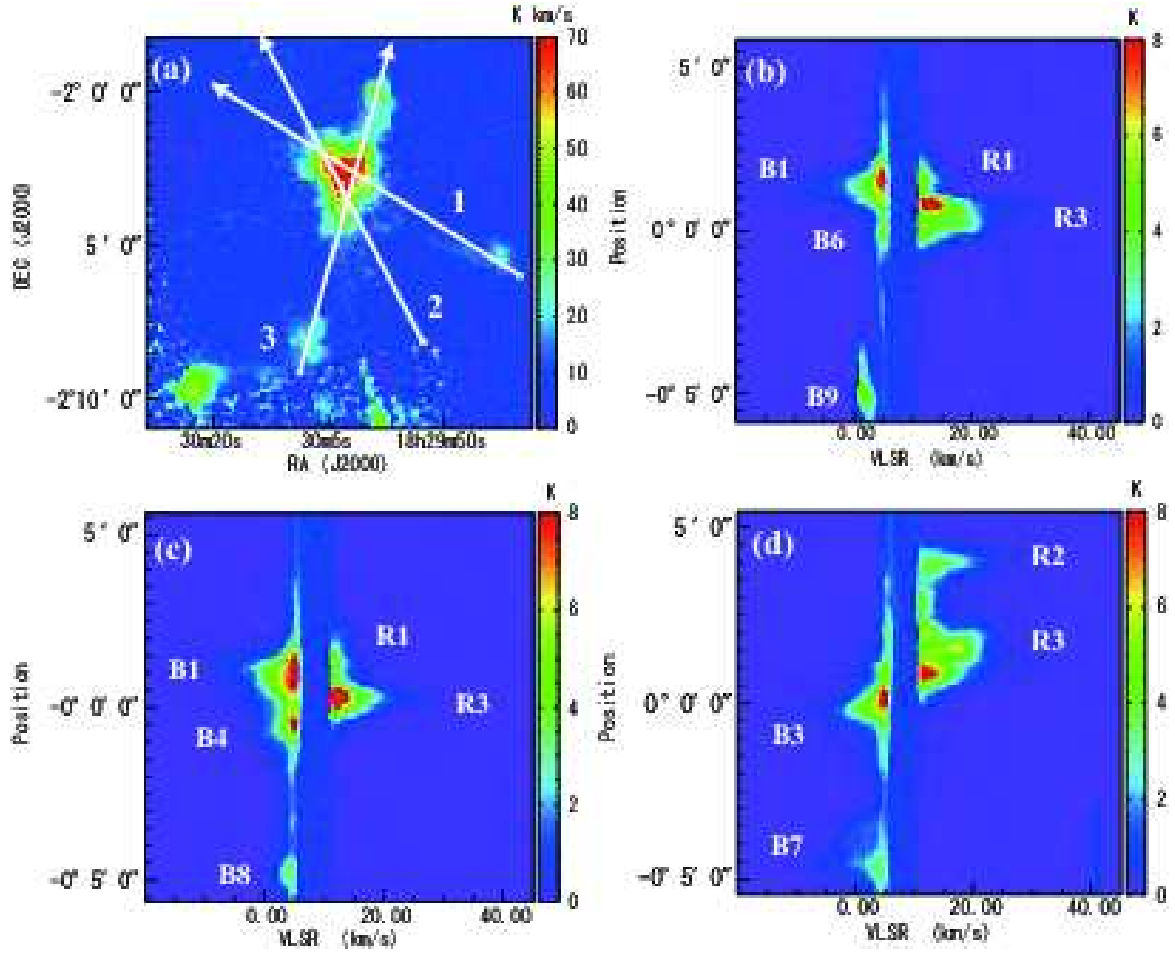


FIG. 17.— (a) Integrated intensity map showing the positions of the PV diagrams. (b) Position-velocity diagram along the line 1 indicated in panel (a). (c) the same as that of panel (b) but for the line 2, (d) the same as that of panel (b) but for the line 3.